Fakultät für Mathematik und Naturwissenschaften | RWTH AACHEN UNIVERSITY

Dynamical Systems and Paradigms for Bio-inspired Computing

Von der Fakultät für Mathematik und Naturwissenschaften der RWTH Aachen University zur Erlangung des akademischen Grades eines Doktors der Naturwissenschaften genehmigte Dissertation

vorgelegt von

Master of Science

Pezhman Ebrahimzadeh

Berichter: Univ.-Prof. Dr. rer. nat. Moritz Helias
Univ.-Prof. Dr. rer. nat. Michael Krämer
Prof. Yuri Maistrenko

Tag der mündlichen Prüfung*: 10.02.2026*

Diese Disseration ist auf den Internetseiten der Universitätsbibliothek online verfügbar.



"We can lift ourselves out of ignorance, we can find ourselves as creatures of excellence and intelligence and skill. We can learn to be free!"

Richard Bach, Seagull Jonathan Livingston



to the memory of my parents
Simin and Dariush

Acknowledgements

In addition to my own hard work and persistence, the completion of the present thesis would not have been possible without the immense support that I have received both professionally and privately. I would like to thank those who contributed to this thesis and my scientific life, in particular Yuri Maistrenko and Michael Schiek for giving me the opportunity to enter the world of nonlinear dynamics and chaos and supported me throughout this journey. I would like to express my special gratitude to Moritz Helias, without whom this thesis would not have came to completion. I would also like to express my gratitude to our collaborators Tomasz Kapitaniak and Jürgen Kurths for their knowledge and experience and Peter Ashwin for insightful discussions.

Finally, I owe lots of gratitude to my friends and family. The support of every single one of you has been very valuable to my completion of this journey. My Brother Shayan who has always been a source of support and my beloved Ziggy whom has always been by my side and whose luminous discussions on nonlinear dynamics and networks encouraged my work.

Fakultät für Mathematik und Naturwissenschaften

RWTH AACHEN UNIVERSITY

Eidesstattliche Erklärung

Declaration of Authorship

I, *Pezhman Ebrahimzadeh*

declare that this thesis and the work presented in it are my own and has been generated by me as the result of my own original research.

Hiermit erkläre ich an Eides statt / I do solemnely swear that:

1. This work was done wholly or mainly while in candidature for the doctoral degree at this faculty and university;

2. Where any part of this thesis has previously been submitted for a degree or any other qualification at this university or any other institution, this has been clearly stated;

3. Where I have consulted the published work of others or myself, this is always clearly attributed;

4. Where I have quoted from the work of others or myself, the source is always given. This thesis is entirely my own work, with the exception of such quotations;

5. I have acknowledged all major sources of assistance;

6. Where the thesis is based on work done by myself jointly with others, I have made clear exactly what was done by others and what I have contributed myself;

7. Parts of this work have been published before, see “Author’s List of Publication”

Aachen, 02.02.2025

Pezhman Ebrahimzadeh

Author's list of publication

The work presented in this thesis is in parts based on the following publications:

Minimal chimera states in phase-lag coupled mechanical oscillators

by Pezhman Ebrahimzadeh, Michael Schiek, Patrycja Jaros, Tomasz Kapitaniak, Stefan van Waasen, Yuri Maistrenko;

published in The European Physical Journal Special Topics 229 (2020): 2205-2214

Parts of this publication enter Chapter 4.

Mixed-mode chimera states in pendula networks

by Pezhman Ebrahimzadeh, Michael Schiek, and Yuri Maistrenko;

published in **Chaos**: An Interdisciplinary Journal of Nonlinear Science 32.10 (2022).

Parts of this publication enter Chapter 2 & 3 and Discussion of the thesis.

Conference contributions

Modified communication architecture for neuromorphic systems

Robert. Kleijnen and Pezhman Ebrahimzadeh, contributed talk, "Networks 2021" conference, virtual (2021).

Chimera States in the Minimal Network of Coupled Pendulum

Pezhman Ebrahimzadeh, Michael Schiek, and Yuri Maistrenko; contributed talk, SIAM (Society for Industrial and Applied Mathematics) conference, virtual (2021).

Chimera states in three coupled metronomes

Pezhman Ebrahimzadeh, Michael Schiek, and Yuri Maistrenko, and S. Van Waasen; contributed talk, School and Workshop on Patterns of Synchrony: Chimera States and Beyond, ICTP, Trieste, Italy (2019).

Abstract

A complex system consists of many interacting elements whose dynamics assumes different spatio-temporal scales, examples of which ranges from neural networks in living matter, neuromorphic computing systems mimicking the brain, coupled memristor systems, conservative and dissipative nonlinear dynamical systems, Earth's climate system, economy, psycho-social phenomenon, and power grid networks, to name a few; nonlinear dynamical systems are of particular interest for modeling of biological, physical and computational systems. In nonlinear dynamical systems, attracting states emerge as long-term behaviors, and multiple attractors can coexist for the same set of system parameters. The emergence and multiplicity of attractors is one of the paradigms how neural networks store patterns as associative memory.

In this thesis, we analyze the emergent dynamical behavior of systems of coupled excitable elements with inertia, pendula networks, and study the effects of coupling on the collective behavior. The counterintuitive network attractors, the chimera states, are observed as frequency clustering of the pendula into synchronous manifolds. The stability of the chimeras, as well as fixed points, are studied for various network sizes. The minimal system composed of three pendula has been extensively studied where three types of distinct chimera patterns are identified, with their respective areas of existence and multiplicity regions are found. The switching dynamics between attractors in the region of multiplicity, driven by input and noise, are qualitatively examined with the hypothesis that this sequence of switchings may serve a role in neural computation. Finally, we discuss the experimental setup of minimal metronome network and the resulting chimera states. In conclusion, this thesis provide insights into the potential of attractor dynamics and switching behaviors in complex systems, suggesting applications for neural computation and advancing our understanding of emergent patterns.

Contents

Acknowledgements **vii**

Abstract **xiii**

1 Neuron and Network Models **7**

1.1 System of Weakly Coupled Neurons 11

1.2 Collective dynamics of Kuramoto model 17

1.3 Summary 20

2 Pendula Networks **21**

2.1 Dynamics of a pendulum $N = 1$ 22

2.2 System of two coupled pendula $N = 2$ 25

2.2.1 Fixed Points 25

2.2.2 Limit Cycles 30

2.3 $N = 3$ and Emergence of Chimera States 34

2.3.1 Fixed Points 34

2.3.2 Limit Cycles and Chimera States 36

2.4 Network of Arbitrary Size N 41

2.5 Summary 45

3 Attractor Networks and Neural Computation **47**

3.1 Introduction 48

3.1.1 Associative memory 49

3.1.2 Physical Realization of NNs and Reservoir Computing 51

3.2 Chimera Networks 54

3.3 Summary 59

4 Model-in-the-loop Experiment **61**

4.0.1 The setup 61

4.0.2 Results 63

5 Conclusion **69**

5.1 Outlook 70

List of Figures

1.1 Anatomy of Neuronl 8

1.2 Limit cycle and canonical model 12

1.3 Chimera state 18

1.4 Traveling chimera state 18

1.5 Phase Transition In Kuramoto Oscillator System 19

2.1 Bifurcation diagram of the pendulum 23

2.2 Stability of asynchronous fixed points 29

2.3 Fixed point profile of the system of two coupled pendula . . . 30

2.4 Stability of $N = 2$ coupled pendula 32

2.5 Topology of the period-doubled limit cycle 33

2.6 Asynchronous fixed points of $N = 3$ pendula network 35

2.7 Parameter region of system behavior with delayed coupling . 38

2.8 Homoclinic Bifurcation, Birth of Limit Cycle and initial state dependency 39

2.9 Dynamical space 40

2.10 Basins of Attraction 40

2.11 Chimera states in network of arbitrary size 42

2.12 Inter-cluster dynamics of mixed-mode chimera states 44

3.1 Cognitive simplification of a concept 48
3.2 Fixed point landscape of Hopfield neural network 50
3.3 Dynamical regimes of logistic map 51
3.4 Attractor network in dynamical space 54
3.5 Attractor network analysis 55
3.6 Excitability of chimera states 56
3.7 Dynamics on the chimera network with driving input 57
3.8 History dependency of the chimera network with temporal driving input 58

4.1 Experimental setup configuration. 62
4.2 Metronome readout coupling structures. 63
4.3 Chimera state in coupled metronome system 64
4.4 Parameter region of system dynamics 66
4.5 Heteroclinic switchings 67

Introduction

The invention of the digital computer marked the dawn of a new era. Ever since, computing devices have been rapidly improving in terms of their speed and accuracy. Such infrastructure has been used for information processing in almost all scientific fields. Although the initial ideas for computer functionality were inspired by the brain [Von Neumann and Kurzweil, 2012], the intrinsic differences, in structure for example [Turing, 2009], leads both not only to be efficient in different areas, but the information processing in the brain of the living creatures with a central nervous system [Brodal, 2004] is different than the computer. Computers are fast and accurate in executing well-defined algorithms, whereas the brain can learn various skills from a minimal fuzzy data set that is potentially an ill-defined problem. An example of which is learning a language without knowing its grammatical structures [Neubauer and Fink, 2009].

The recent advances in artificial intelligence, specifically artificial neural networks (ANNs), virtually enhanced the computer's ability for human-efficient tasks emulating the structure and functionality of biological neural networks. A network composed of neuron-like elements, such as spiking neuron models or their statistical-averaged forms, functions as a core computational unit that runs on a conventional computer architecture [Lek and Park, 2008].

After the success of digital computers, *neuromorphic computing* has been a considerable approach to computing that mimics the human brain structure and functionality. It originates back in the 1980s when [Mead, 1990] and [Mahowald and Mead, 1994] developed the first silicon retina and silicon neuron/synapse. At the present, neuromorphic computing entails designing hardware and software that simulate neural and synaptic activity for information processing, including analog and digital VLSI systems, threshold switches and memristor networks, ANN training accelerator hardware, event-based cameras, to name a few.

Despite the attempts at designing dedicated hardware infrastructures suitable for neural network operations, that is neuromorphic computing,

in practice simulation and computation in large networks comparable to human-sized brain remains fundamentally difficult due to large data communication, energy consumption and slow time acceleration factors [van Albada et al., 2018]. In the conventional computers, the data communication problem is due to the von Neumann architecture [Arikpo et al., 2007] that separates the memory and the computing units (CPU). With every clock update in the computer the data processing happens synchronously, that is all the data need to be transferred into the CPU, where the computation is carried out and the processed data are transferred back to the memory unit. In the neuromorphic computing devices, aside from the physical limitations of manufacturing a three dimensional brain structure on a two dimensional electronic wafer, our lack of knowledge on the nature of the memory and computation prevents us from leaving the realm of von Neumann architecture.

Reservoir computing [Nakajima and Fischer, 2021] was introduced as a paradigm shift for learning/computation in the artificial neural networks by using the dynamical properties of a physical medium as its computation substrate. It was proven that, under certain conditions for the computation substrate, the reservoir linearizes the input data by mapping it into a higher dimensional space, making it possible for a faster learning process. The mapping can be done statistically (*echo-state* network [Lukoševičius and Jaeger, 2009]) or with sequence of dynamical patterns (*liquid-state* machine [Maass et al., 2002]). The intrinsic dynamics of the reservoir, however, is generally treated as a black box.

To uncover the functionality of the computing substrate of the reservoir, for example, the nature of memory and computation and their entanglement, one may start considering various networks of coupled excitable elements that compose nonlinear dynamical systems [Strogatz, 2018]. The intrinsic dynamics of such networks include fixed point, limit cycle and chaotic regimes [Brezetsky et al., 2021a, Sprott, 2008]. Each of these regimes have been employed in neural computation [Khona and Fiete, 2022]. Some early circuit-level brain function models concerning *associative memory*, classic Hopfield networks [Hopfield, 1982] for example, encode the data as spatially distributed stable patterns of activity that can be reduced to a fixed point attractor description. These fixed point attractors are generally constructed by modification of the connection weights between the network elements, i.e., the artificial neurons. In contrast, some cognitive processes such as reasoning and decision-making, operate with temporally-coded information known as *working memory* [Miyake et al., 1999]. The dynamical property of the working memory consists of short-lived but persistent neural activity correlated to that of a terminated input [Compte, 2006, Szatmáry and Izhikevich, 2010]. It has been proposed that, limit cycle regime attractors such as *bump states* [Laing and Chow, 2001], may describe mechanisms

of the working memory [Laing et al., 2002, Wimmer et al., 2014]. Although chaotic attractors may not be biologically plausible, neural networks can inhibit and utilize chaotic attractors for faster computation [Hirsch and Baird, 1995, Klotz and Bräuer, 1999, Schuecker et al., 2018]. Furthermore, a comprehensible field-theoretic study for the neural networks can be found in [Helias and Dahmen, 2020]

In this work, we study the emergence and existence regimes of various attractors in a network of globally coupled oscillators. The attractors consist of trivial and non-trivial fixed points, classical [Kuramoto and Battogtokh, 2002, Abrams and Strogatz, 2004, Ashwin and Burylko, 2015] and mixed-mode chimera states [Ebrahimzadeh et al., 2022] as distinguished frequency clusters and switching dynamics between such chimera states. The oscillator model we use is pendulum equation, that is paradigmatic model for an excitable phase oscillator, equivalent to the theta neuron model. [Ermentrout and Kopell, 1986]. In contrast to its canonical counterparts, the pendulum equation includes an additional "bistability" [Belykh et al., 2016] region of coexistence of the equilibrium and limit cycle due to homoclinic bifurcation. In turn, the coupled pendula network inherits multistability which allows for coexistence of several attractors.

In Chapter 1 canonical model for weakly coupled spiking neural networks are discussed. The collective dynamics are analyzed and chimera states are introduced as nontrivial steady solutions in a network of phase oscillators emerging due to coupling effects including phase-shift.

In Chapter 2, we introduce the pendulum equation as a modified variation of the canonical spiking neuron models that relaxes the weak coupling condition in spiking neural networks. A detailed study of the dynamical behavior of the various pendula networks of different sizes is carried out. Mixed-mode chimera states that are manifested as combinations of frequency clusters are identified as attractor states in pendula networks. Emergent mechanism, bifurcation types, and coexisting condition of the chimera states are analyzed. Due to the system multistability, various chimera states may coexist at the same system parameters leading to the chimera network, an attractor network in the system phase space.

In Chapter 3, the virtual realizations of associative and working memory in a physical medium are shortly discussed. The chimera network is instigated, including a qualitative study of its topological properties, as an ensemble of attractors capable of encoding associative memory. We conclude the chapter with the conjecture that a chimera network can be used as a dynamical medium linking associative to working memory with the sensitivity that allows for the preservation of the temporal encoding of the data in spike trains.

In Chapter 4, we present the experimental setup of the minimal metronome network and the results of direct numerical study and experiment including the weak chimera states.

Chapter 1

Neuron and Network Models

According to the classical doctrine in biology, animals possess a highly complex entity - the nervous system - which coordinates sensory information gathered from the environment. At the top of the nervous system hierarchy is the brain [Brodal, 2004]. It was not until 1900s that the study of the brain with detailed biological methods identified its building blocks, the neurons [y Cajal, 1909]. The number of the neurons varies dramatically across species: 300 billion in African elephants, 10-20 billion in human cerebral cortex and down to only 302 in C.elegance worm [Williams and Herrup, 1988]. The building blocks of the brain, however, exhibit similar structure and almost identical functionality across animals, hinting towards a universal concept of the brain as the main computational organ composed of neurons in the body [López-Muñoz et al., 2006]. In the 1930s, the concept of chemical transmission of nerve pulses across the neurons was discovered [Loewi, 1945], followed by the electrical communication mechanism of the action potential between the neurons [Eccles, 2013].

Important morphological aspects of neurons include dendrites that receive inputs from other neurons, a core body, and the axon that carries the neuronal output to other cells, Fig. 1.1. A dendrite tree may include thousands of synapses with high number density in the tree space while axon may extend to large fractions of the brain. For example, the mouse brain axon extends 40mm. Moreover, neurons include a wide variety of membrane-spanning ion channels that control the ionic flow across the cell membrane, including, predominantly, sodium (Na^+), potassium (K^+), calcium (Ca^+) and chloride (Cl^-). Due to the gate mechanism of the ionic channels, a neuron membrane maintains a voltage gradient compared to its surrounding, of about $V_0 = -70$ mV, hence the cell is said to be polarized. Current flowing into the cell (stimuli), changes the membrane potential to less negative or positive, depolarizing the neuron. If a depolarization is suf-

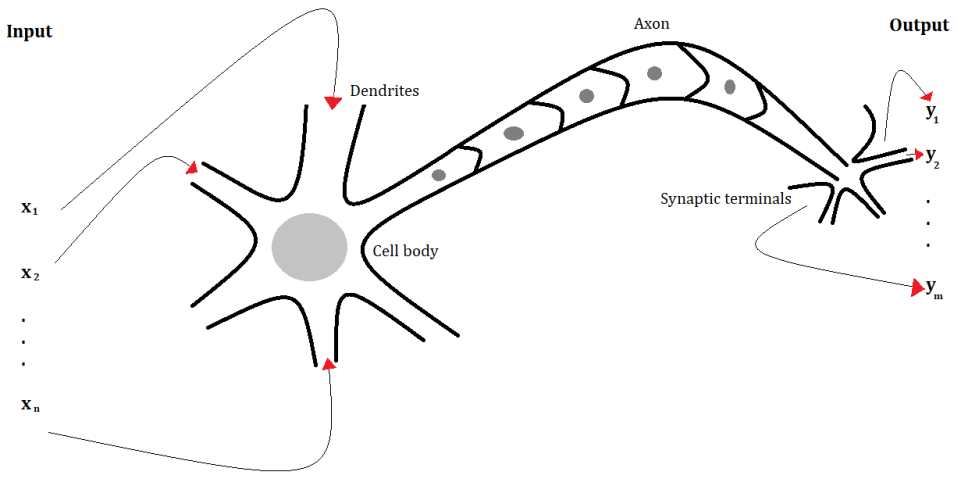

Figure 1.1: Anatomy of Neuron.

ficiently large to raise the membrane potential above a certain threshold, the neuron generates an action potential, usually roughly about 100 mV. The action potential then propagates via the axon to synapses. The main importance of the action potential is that it can travel over large distances rapidly without attenuation, whereas subthreshold fluctuations are severely attenuated over distances of 1mm or less. Due to their narrow shape with respect to time,the action potential is also called a *spike* and is modeled with Dirac's delta function. The main communication of the action potential is via the chemical synapses which enable long range, lossless interaction between neurons. The second most important communication mechanism is via electrical synapses, which involves mechanical and electrical conductive link between neighboring neurons. Compared to chemical synapses, electrical ones are much faster in communicating the nerve impulses, albeit with a shorter effective range, about $3 - 4$ nm.

Neurons typically respond to stimuli by producing complex spike sequences that reflect both intrinsic dynamics of the neuron and temporal characteristics of the stimuli [Dayan and Abbott, 2005]. The mapping between the stimulus to neural response is called *neural encoding*, and serves as the basis for computation schemes in brain. For example, a naive form of encoding information in neural response would be the time interval between the spikes. Understanding the intrinsic dynamics of the neurons (neuron models), hence, has become a vital component in the study of neural networks and the brain.

Spiking neuron models generally formulate neuron dynamics by describing the membrane voltage as a function of the input currents (stimuli)

and the activation of the ion channels. Such models can be divided into several categories: comprehensive and data driven models explaining the neuron and brain dynamics based on observation and experiments, and empirical/canonical models capturing one or a few important neuro-biological observables [Hoppensteadt and Izhikevich, 1997]. The difficulty with the first category is that, despite capturing substantial aspects of neuro-dynamics, they fail to account for areas where data are unknown; moreover, they are not easily amenable to mathematical analysis. A famous example of such a neuron model category is the Hodgkin-Huxley (HH) model. Contemporary modified versions of the HH model can include more that 20 tuning channel parameters. The simplified empirical models, however, are more suitable for system analysis without a full knowledge of the detailed dynamics of the system. In this sense, for example, bifurcations in brain dynamics can be studied with canonical models, which operate in the critical regime. The drawbacks of this appraoch is that the models might overlook some aspect that are otherwise important, in other words, the model would be oversimplified.

The essential, excitable dynamics of a spiking neuron consists of *rest*, *excited* and *refractory* states. An uncoupled/unperturbed neuron always persists in a rest state with an ionic polarization that characterizes its membrane potential V_0. After receiving an input current (perturbation), depending on whether the input is sub- or supra-threshold, the system either has a small-amplitude/subthreshold response or emits an action potential in the form of a spike.. After the emission of a spike, the neuron enters a short refractory state, recovering its ionic polarization and reseting into rest potential V_0. Notably, a neuron cannot emit another spike while in the refractory state. Moreover, depending on the neuron type, the spike firing rate is a function of the input. This information is enough to formulate a model of spiking neurons. An excitable neuron lies in the rest state, corresponding to a stable fixed point or equilibrium. A continuously spiking –without external input– neuron is in the limit cycle (periodic orbit) regime.

From a mathematical point of view, an excitable neuron model, is a bifurcation characterized by separation of the rest state and sustained oscillatory motion which is the necessary condition for observing excitable behavior Rinzel and Ermentrout [1998]. In this sense, the threshold is not a point, but rather a manifold whereby the mechanism of the threshold-like behavior depends on the geometric structure of the phase space. In order to be able to formulate a mathematical formalism for spiking neurons, we introduce some mathematical definitions [Kuznetsov et al., 1998].

Definition: A dynamical system is a triple $\{T, X, \phi^t\}$, where T is a time set, X is a state space, and $\phi^t : X \to X$ is a family of evolution operators parameterized by $t \in T$, such that for some initial state $x_0 \in X$ the state at

some time t is given by $x_t = \phi^t x_0$.

Subsequently, a time continuous dynamical system can be represented as a system of ordinary differential equations

$$\dot{X} = F(X),\ X = (X_1, ..., X_m)^\top \in \mathbb{R}^m. \tag{1.1}$$

A *flow* or an orbit of a dynamical system (1.1) is a family of time operators $\{\phi^t\}$ such that $X(t) = \phi^t(X_0)$ is a solution of the system starting from X_0; that is

$$\frac{\mathrm{d}\phi^t(X_0)}{\mathrm{d}t}|_{t=\tau} = F(\phi^\tau(X_0)),\ \phi^0(X_0) = X_0. \tag{1.2}$$

Definition: A cycle is a periodic orbit, namely a non-equilibrium orbit L_0, such that each point $x_0 \in L_0$ satisfies $\phi^{t+T_0} = \phi^t x_0$ with some $T_0 > 0$ for all $t \in T$.

Definition: A cycle of a continuous-time dynamical system, in a neighborhood of which there are no other cycles, is called a limit cycle γ.

Definition: Two dynamical systems

$$\dot{X} = F(X), X \in \mathbb{R}^m, \text{ and } \dot{Y} = G(Y), Y \in \mathbb{R}^m, \tag{1.3}$$

are said to be topologically equivalent if there is a homeomorphism $h : \mathbb{R}^m \to \mathbb{R}^m$ taking each orbit $\phi^t(X)$ of one of the systems to an orbit $\psi^t(Y)$ of the other one $h(\phi^t(X)) = \psi^{t_1}(h(X))$. Two dynamical systems have qualitatively similar behavior if they are topologically equivalent. On the other hand, when h is not a homeomorphism, dynamical system $\dot{Y} = G(Y)$ is said to be a model of $\dot{X} = F(X)$. In this case Y usually belongs to a space smaller than $\mathbb{R}^m$.

To apply the above definitions to practical terms, sustained spiking behavior is locally topologically equivalent to a limit cycle in the neuron's dynamical space. A regular (tonic) spiking pattern can be understood, for example, when the neuron's dynamics has fallen into the limit cycle. In general, such a limit cycle can coexist with the equilibrium, which is equivalent to the rest state, and different spike patterns then would correspond to neuron visiting each of these attractors; a simple example of such spike pattern is bursting, where visit to each of the attractors happens regularly.

Another aspect of neuro-dynamics that a neuron model should incorporate the mechanism by which a neuron is excitable and emits spikes. The excitability types based on Hodgkin's experimental findings and the mathematical explanation of Rinzel and Ermentrout, are

1. **Type I excitability**, which the firing rate (or frequency) of the neuron continuously increases as the magnitude of the input increases; and

2. **Type II excitability** with a discontinuous jump in the neuron firing rate.

The two excitability types are explained by the bifurcations according to which the equilibrium vanishes and the limit cycle is born. In the Type I, there are two fixed points, a stable node and a saddle, on an invariant circle. The equilibrium includes stable manifolds while the saddle has a stable and an unstable manifold. Before the bifurcation, in the fixed point regime, the stable node attracts all the nearby initial states. Following a perturbation, the trajectory would either end up directly in the equilibrium if the perturbation happens on the stable manifold, or may go around on the invariant circle to reach the equilibrium if the perturbation happens on the unstable manifold. The latter corresponds to emission of a single spike. At the bifurcation, the saddle and the equilibrium collide and annihilate and the invariant circle becomes homoclinic orbit to the saddle-node. The period of this orbit is infinite (frequency is zero). In the Type II excitability, the stable fixed point changes its stability in a Hopf bifurcation, and a small amplitude limit cycle emerges.

1.1 *System of Weakly Coupled Neurons*

In the previous section, we discussed the fundamental aspects of neurodynamics, such as threshold behavior and spiking patterns of a single neuron. In the following, a framework for obtaining the dynamical behavior of the neurons in the presence of weak coupling is discussed. Within this framework, Nm differential equations describing the system dynamics are reduced to N first-order differential equations.

A system of weakly coupled neurons can be formulated as

$$\dot{x}_i = f_i(x_i) + \sigma g_i(x_1, ..., x_n, \sigma),\ i = 1, ..., n. \tag{1.4}$$

Here, $x_i \in \mathbb{R}^m$ is the activity (including the action potential V) of the ith neuron with its dynamics governed by f_i, and g_i describes the connections of the other neurons towards neuron i. Moreover, the strength of the synaptic connections are described by the dimensionless parameter $\sigma \ll 1$. Weakly connected systems have been of interest since seventeenth century, when Huygens studied synchronization in a pair of pendulum clocks. Later on, systems in the form of Eq. (1.4) have been extensively studied , for example in formal perturbation theories developed by Poincare, Lyapunov and Malkin, and averaging theories by Bogoliubov and Mitropolsky.

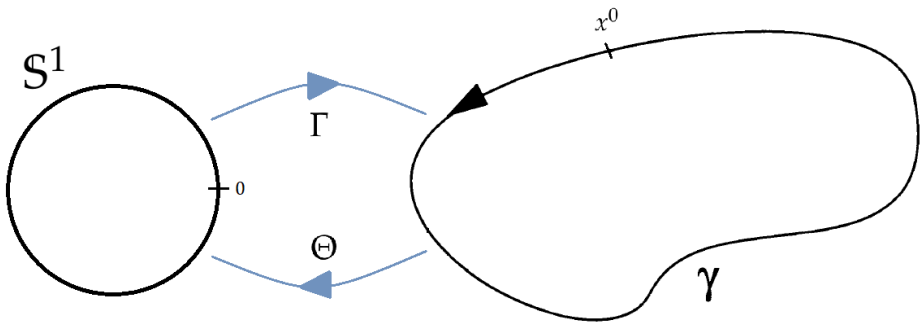

Figure 1.2: Limit cycle γ equating the firing of a neuron in $\mathbb{R}^m$ can be locally reduced to dynamics on an invariant circle $\mathbb{S}^1$.

The canonical model describing the essential dynamics of a spiking neuron can be understood as a phase equation where the neuron model parameters are reduced to a phase parameter. In this sense, there exists a limit cycle attractor γ which describes the spiking behavior, and γ is homeomorphic to the unit circle $\mathbb{S}^1$. Let $x^0 \in \gamma$ be a zero phase point and $x(t)$ be the periodic solution to $\dot{x} = F(x, \lambda)$ such that $x(0) = x^0$. Moreover, let $\theta(t) \in \mathbb{S}^1$ be a phase variable that rotates with constant speed ω, that is $\theta(t) = \omega t$. Then, there exists a natural parametrization with mapping $\Gamma : \mathbb{S}^1 \to \gamma$ such that

$$\Gamma(\theta(t)) = x(t) \in \gamma, \;\; t \in [0, 2\pi/\Omega]. \tag{1.5}$$

The existence of such homeomorphic mapping between a limit cycle and the unit circle $\mathbb{S}^1$ paves the way for the modeling of a network of weakly coupled limit cycle (spiking) neurons to their relative phase reduced forms.

Hoppensteadt and Izhikevich [1997] offer the following

Theorem: consider a family of weakly connected systems

$$\dot{X}_i = F_i(X_i, \lambda) + \sigma G_i(X, \lambda, \sigma), \;\; i = 1, ..., n, \tag{1.6}$$

where $X_i \in \mathbb{R}^m$, and the uncoupled system ($\sigma = 0$) has an exponentially orbital limit cycle attractor $\gamma_i \subset \mathbb{R}^m$ with frequencies $\Omega_i(\lambda) \neq 0$. The local model of (1.6) is the dynamical system

$$\dot{\theta}_i = \Omega_i(\lambda) + \sigma g_i(\theta_1, ..., \theta_n, \lambda, \sigma), \;\; i = 1, ..., n, \tag{1.7}$$

on the n-torus $\mathbb{T}^n = \mathbb{S}^1 \times ... \times \mathbb{S}^1$ and with $\theta_i \in \mathbb{S}^1$.

The complete proof of this theorem can be found in Hoppenstead and Izhikevich, however we will discuss some necessary steps towards the proof.

Suppose each equation in the uncoupled system ($\sigma = 0$) $\dot{X}_i = F_i(X_i)$ has a stable normally hyperbolic compact invariant manifold $M_i \subset \mathbb{R}^m$ such that their product $M = M_1 \times ... \times M_n$ is normally hyperbolic. Then the weakly connected system

$$\dot{X}_i = F_i(X_i) + \sigma G_i(X, \sigma), \tag{1.8}$$

has a local model

$$\dot{x}_i = F_i(x_i) + \sigma \tilde{G}_i(x, \sigma), \quad x_i \in M_i. \tag{1.9}$$

That is, there is an open neighborhood W of M and a continuous function $\tilde{h}_\sigma : W \to M$ that maps solutions of the (1.8) to those of (1.9).

For a system of all spiking neurons Eq. (1.6), the hyperbolic invariant manifolds M_i are the limit cycle γ_i, with each γ_i having the parametrization Γ_i Eq. (1.5). We have

$$\dot{x}_i = \frac{\mathrm{d}\Gamma_i(\theta_i)}{\mathrm{d}t} = \frac{\mathrm{d}\Gamma_i(\theta_i)}{\mathrm{d}\theta_i}\dot{\theta}_i = \Gamma_i'(\theta_i)\Omega_i = F_i(\Gamma_i(\theta_i(t))), \tag{1.10}$$

for all t. Inserting this condition into Eq. (1.6), one arrives at the phase equation

$$\dot{\theta}_i = \Omega_i + \sigma a_i(\theta_i)\tilde{G}_i(\Gamma(\theta), \sigma) \tag{1.11}$$

such that

$$a_i(\theta_i) = \frac{\Omega_i F_i(\Gamma_i(\theta_i))^\top}{|F_i(\Gamma_i(\theta_i))|^2} \tag{1.12}$$

and $g_i(\theta_1, ..., \theta_n, \lambda, \sigma) = a_i(\theta_i)\tilde{G}_i(\Gamma(\theta), \sigma)$. Hoppenstead and Izhikevich showed that a function $h : W \to \mathbb{T}^n$ that maps solutions of Eq. (1.6) to that of phase equation (1.7) exists and is a composition of $\tilde{h}_\sigma$ and Γ^{-1}. In other words, the phase equation is locally topologically equivalent and the phase equation is a *model* of system (1.6).

The phase model Eq. (1.11) describes the dynamics of the system when the dynamics of each neuron lies exactly on the periodic solution γ, hence any deviations from γ are not incorporated, that is, $\Gamma'(\tilde{\theta}) = 0$ for any $\tilde{\theta} = \Gamma^{-1}(x)$, $x \notin \gamma$.

The most important role of a neuron model is to describe the neuro-dynamics and response to stimuli. The same is expected from a neural network; the intrinsic dynamics of the network is, however, much more intricate than that of a single neuron due to the presence of many nonlinearities associated with the couplings, in addition to the already complex neuro-dynamics. Since the phase equation formalism is topologically equivalent to the respective neuron model, one can investigate the intrinsic (and stimulated) dynamics of a neural network via the phase equations. To that

end, we introduce the famous *Malkin's theorem for weakly coupled oscillators* is followed by Kuramoto's model and explicit forms of coupling. We note that, the term "weak coupling" does not necessarily imply small coupling strength, but rather that the oscillators intrinsic dynamics dominate the effects due to coupling at each point in the limit cycle. Mathematically, over a given period $|f_i(x_i)|$ should be greater than $|\sigma g(x, \sigma)|$ by at least an order of magnitude.

Malkin's Theorem Consider a weakly coupled system $\dot{X}_i = F_i(X_i) + \varepsilon G_i(X)$ such that each equation in the uncoupled system ($\varepsilon = 0$) has an exponentially orbitally stable 2π-periodic solution $\gamma_i \subset \mathbb{R}^m$. Let $\tau = \varepsilon t$ be slow time and $\phi_i(\tau) \in \mathbb{S}^1$ the phase deviation from the natural oscillation $\gamma_i(t)$. Then, the vector of phase deviations $\phi = (\phi_1, ..., \phi_n)^\top \in \mathbb{T}^n$ is a solution to

$$\phi_i' = H_i(\phi - \phi_i, \varepsilon), \quad i = 1, ..., n, \tag{1.13}$$

where $' = \mathrm{d}/\mathrm{d}\tau$, the vector $\phi - \phi_i = \phi = (\phi_1 - \phi_i, ..., \phi_n - \phi_i)^\top \in \mathbb{T}^n$ and

$$H_i(\phi - \phi_i, 0) = \frac{1}{2\pi} \int Z_i(t) G_i(\gamma(t + \phi - \phi_i)) \mathrm{d}t, \tag{1.14}$$

where $Z_i(t) \in \mathbb{R}^m$ is the unique nontrivial 2π-periodic solution to the linear system

$$\dot{Z}_i = -\Big(DF_i(\gamma_i(t))\Big)^\top Z_i, \tag{1.15}$$

satisfying the normalization condition

$$Z_i(0)^\top F_i(\gamma_i(0)) = 1. \tag{1.16}$$

We note that $DF_i(\gamma_i) = \nabla F_i(X)|_{X=X_i^\gamma}$ is the directional derivative. Moreover, solution $Z_i(t)$ to the adjoint problem Eq. (1.15) is the phase sensitivity function of oscillator x_i evaluated on the limit cycle γ_i.

The response of a limit cycle to infinitesimal perturbations simplifies the form of phase sensitivity function to the so called *phase response curve* (PRC), [Gutkin et al., 2005]. To that end, we need to carefully define the *attractor* property.

Definition: γ is an attractor, if for each $\tilde{x}$ sufficiently close to γ ($\tilde{x} \in \mathfrak{B}_\gamma$), the time evolution of $\tilde{x}$ approaches the attractor, that is $\|\phi^t(x^\gamma) - \phi^t(\tilde{x})\| \to 0$ as $t \to \infty$.

The set $\mathfrak{B}_\gamma$ is called the basins of attraction for the attractor γ. Among the subsets of the basins of attraction, there is an important sub-manifold $\mathfrak{I}(\theta)$, such that for $x \in \mathfrak{B}$ have the same asymptotic phase $\Theta(x) = \theta$, where $\Theta : \gamma \to \mathbb{S}^1$ maps the limit cycle onto the invariant unit circle. The set $\mathfrak{I}(\theta)$ is called the isochron associated with phase θ, $\mathfrak{I}(\theta) = \{x \in \mathfrak{B}_\gamma | \Theta(x) = \theta\}$.

In general, isochrons are shown [Monga et al., 2019] to exist for any stable hyperbolic periodic orbit and their union spans the whole area of basin of attraction $\mathfrak{B}_\gamma$. The topological illustration of the isochrons would be curves transversal to the limit cycle. For any infinitesimal perturbation there can be found an isochron curve that will reset the phase. The phase response curve then quantifies the extent to which the perturbation advances or pushes back the limit cycle. In other words, if the perturbation is in the direction of the rotation of the limit cycle, the new limit cycle will have a phase advance compared to the old one proportional to the PRC. On the other hand, if the perturbation is in the opposite direction to the rotation of the limit cycle, there will be a phase delay. The other directions on the planar space are averaged out due to the isochron curve, and the PRC reads $Z_i(\theta) = \nabla\Theta(x)|_{x=x^\gamma(\theta)}$.

As discussed earlier, the dominant communication form between neurons is via the action potential that travels through chemical synapses, followed by the second dominant form of electrical synapses.The model of the neural network and it's phase model do not involve specific assumptions about the synaptic couplings. Through Wick's theorem [Zinn-Justin, 2021] it can be shown that only a pairwise coupling structure contributes to the dynamics while higher order interactions are negligible, $g_i(x_1, ..., x_n) = \sum_{j=1}^{n} g_{ij}(x_i, x_j)$. With this in mind, the phase model of system (1.4) is provided by Winfree oscillators [Winfree, 1967]

$$\dot{\theta}_i = \omega_i + \mu Z(\theta_i) \sum_{j=1}^{n} g_{ij}(\theta_i, \theta_j). \tag{1.17}$$

Using either Malkin's theory or the averaging theory for connect systems, and the linear phase sensitivity function, the phase model reads [Pietras and Daffertshofer, 2019]

$$\dot{\theta}_i = \omega_i + \frac{\mu}{n} \sum_{j=1}^{n} H_{ij}(\theta_j - \theta_i), \tag{1.18}$$

with the coupling function H_{ij} obtained by Eq. (1.14). In a network of identical (or almost identical) neurons, it is safe to assume that the form of interaction would be similar, if not the same, across the network. Hence, one can decompose the coupling interaction into function and network structure $H_{ij}(\chi) \to a_{ij}H(\chi)$. The matrix $[A]_{ij} = a_{ij}$ is the adjacency matrix with entries $a_{ij} = 1$ or 0, for connected and unconnected neurons i and j, respectively. Kuramoto [Ref] showed that, in a network with all-to-all connection, coupling form $H(\chi)$ is an odd function and can be represented by a Fourier series on $\mathbb{S}^1$

$$H(\chi) = \sum_{k=1}^{\infty} b_k \sin k\chi. \tag{1.19}$$

Moreover, Kuramoto suggested that the first harmonic b_1 is dominant and the rest of the series can be disregarded. Finally, we arrive at the Kuramoto model

$$\dot{\theta}_i = \omega_i + \frac{\mu}{n} \sum_{j=1}^{n} \sin(\theta_j - \theta_i - \alpha), \tag{1.20}$$

where α is a phase parameter incorporating the phase-delay or advance of the oscillator with respect to the perturbation.

The approximation (1.17) was obtained under the assumption that a limit cycle γ_i is always an isolated attractor for weak perturbations that span the basin of attractions of γ_i. In order to finalize the phase model equation, one needs to find the phase sensitivity function $Z(\theta)$ for each neuron model. Different phase sensitivity functions can be found in [Brown et al., 2004].

The PRC method, however, is a first order approximation that fails to account for the non-uniformity of the basins of attraction where perturbations of same magnitude will have different effects on the limit cycle and the transient behavior of the system. In order to understand such detail, more correction terms are needed to approximate the limit cycle's response to perturbations. To this end, we briefly discuss the augmented phase reduction for a single neuron where the additional correction term is added as a first-order differential equation. An explicit formulation of the augmented phase reduction in a network remains for future work.

Firstly, we establish the Poincare map P on γ_i: $P : \gamma_i \to \gamma_i$. The new set of coordinates ψ_i are introduced to measure the effects of perturbations in driving the trajectory away from the periodic orbit

$$\psi_i(x) = \lim_{j\to\infty} \left[e_i^T V^{-1} (x_\gamma^j - x_0) exp(-\log \lambda_i t_\gamma^j / T) \right]. \tag{1.21}$$

Here x_γ^j and t_γ^j are defined to be the position and time of the jth crossing of the γ and $e_i^T V^{-1}$ is a left eigenvector of the militarization of the Poincare map near x_0. Moreover, eigenvalues λ_i are the Floquet multipliers of the periodic orbit. It is straightforward now to calculate the augmented phase reduction for a single limit cycle

$$\dot{\theta} = \omega + Z(\theta, \psi) I, \tag{1.22}$$
$$\dot{\psi} = k\psi + R(\theta, \psi) I, \tag{1.23}$$

where $k = \log \lambda_i / T$ is the Floquet exponent and I is the input. The phase response function $Z(\theta, \psi)$ now includes the sensitivity in transversal direction to the limit cycle along side isostable response function $R(\theta, \psi)$ [Monga et al., 2019].

1.2 *Collective dynamics of Kuramoto model*

A major advantage of the phase models is that they allow for a rigorous mathematical analysis of a complex dynamical system and the relation between microscopic states that give rise to collective emergent behaviors.

The Kuramoto model has been used as a minimal mathematical model for investigating the emergence of collective dynamics of limit cycle oscillators and has been subject of intensive studies for the past five decades. At the beginning of the millennium, the chimera states discovered by Kuramoto and Battogtokh [Kuramoto and Battogtokh, 2002] were among the most peculiar and non-intuitive macroscopic behavior found in a network of coupled oscillators. The Kuramoto model for a network of N non-locally coupled oscillators read

$$\dot{\phi}_i = w_i + \frac{\mu}{2r} \sum_{j=i-r}^{i+r} \sin[\phi_j - \phi_i - \alpha], \;\; i = 1, ..., N \tag{1.24}$$

where ϕ_i is the phase parameter of the i'th oscillator, w is the natural frequency and μ is the coupling strength. Moreover, r measures the range of coupling, such that $r = 1$ characterizes the next neighbor and $r = N/2$ is the all-to-all coupling. The phase advance or phase delay response of the target oscillator i to the effect of jth oscillator is captured by α. A phase advance can be understood in the oscillator's phase space when the perturbation displaces the oscillator's phase in the direction of motion, consequently, a phase delay happens when the perturbation is in the opposite direction to the the oscillator's trajectory.

For the case of identical oscillators $w_i = w$, chimera states reported for system (1.24) manifest as coexistence of two groups of synchronous and incoherent oscillators as a results of spontaneous symmetry breaking. The two groups can be distinguished by their average frequency. A typical example of chimera states is presented in Fig. 1.3 for network of $N = 50$ coupled Kuramoto oscillators with coupling range $r = 17$, phase-delay $\alpha = 1.45$, coupling strength $\mu = 0.5$ and natural frequencies $w = 0$. Fig. 1.3 (left) shows the frequency time series of all (top) and two samples of each group (bottom) of oscillators, while the average frequency profile exhibits the famous "bell shape" characteristic.

The mechanism behind this type chimera state can be understood by first analyzing the system symmetries. System (1.24) inherits an S_r symmetry due to coupling radius and identical oscillators. The tendency of this system would be to have a synchronous collective behavior by creating a self-consistent *field* that acts as the synchronizing force. For $\alpha = 0$ the sym-

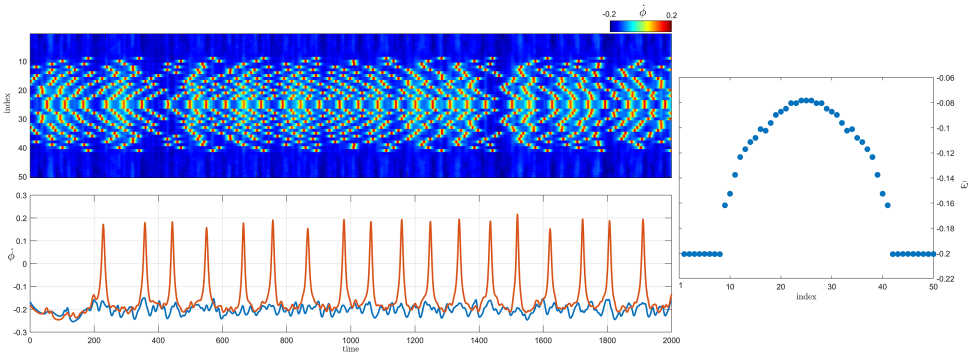

Figure 1.3: Chimera state in Kuramoto system Eq. (1.24) for $N = 50$ identical oscillators with local coupling range $r = 17$. (top) Color-map of velocities where the outer oscillators (in dark blue) are synchronized and the middle group is incoherent. (bottom) Detailed velocity time series of two sample oscillators from synchronous group $i = 1$ and incoherent group $i = 11$. (right) average frequency profile of the system exhibiting the "bell shape" frequency distribution. System parameters are set $\alpha = 1.45$ and $\mu = 0.5$.

metry is retained and the synchronous state prevails; increasing α, however, subverts the action of the field resulting in partial synchronization of the oscillators. The significance of the chimera states lies in the fact that they appear via spontaneous symmetry breaking in a highly symmetrical system.

The dynamics of the Kuramoto phase oscillators in a network of non-identical elements also reveals important aspects of network behavior. The

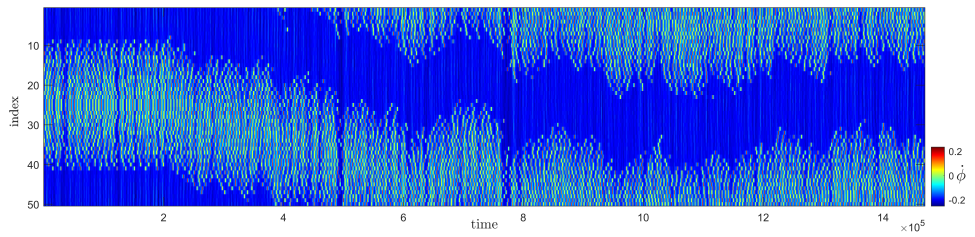

Figure 1.4: Due to finite size effects, the chimera state with the setting presented in Fig. 1.3 loses the spatial stability with oscillators changing between the two synchronous and incoherent groups, the chimera state appears to be traveling.

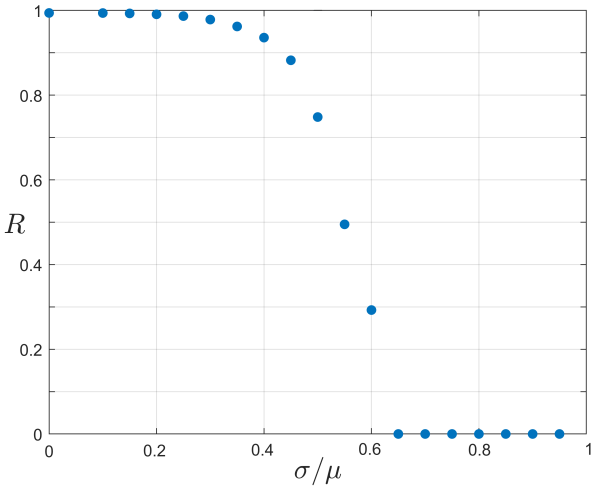

Figure 1.5: Phase transition diagram of the synchronization in the Kuramoto model Eq. (1.25). The natural frequencies are chosen from a normal distribution $\mathcal{N}(\sigma, 1)$.

system of globally coupled oscillators can be written

$$\dot{\phi}_i = w_i + \frac{\mu}{N}\sum_{j=1}^{N}\sin[\phi_j - \phi_i - \alpha],\ \ i = 1, ..., N \tag{1.25}$$

where the values of natural frequencies w_i is drawn from a normal distribution $g(w)$. The extent of synchronization is measured by the order parameter

$$R\exp(i\Theta) = N^{-1}\sum_{j=1}^{N} e^{i\phi_j}. \tag{1.26}$$

The magnitude of R represents the level of synchronization, $R = 1$ for fully synchronized state and $R = 0$ for an incoherent state. The phase parameter Θ then represents the average phase that behaves monotonically $\Theta = \Omega t$ where Ω is the average frequency. Inserting condition (1.26) into Eq. (1.25) yields the self-consistent equation of the oscillator network, assuming parameters R and Ω are constant in time

$$\dot{\psi}_i = w_i - \Omega - \mu R\sin\psi, \tag{1.27}$$

where $\psi_i = \phi_i - \Omega t + \alpha$. Eq. (1.27) is the *active rotator* equation which has two set of solutions consisting of a fixed point (for $|\frac{w_i-\Omega}{\mu R}| < 1$) and limit cycle (for $|\frac{w_i-\Omega}{\mu R}| > 1$). The fixed point solution of Eq. (1.27) corresponds to the synchronized oscillators rotating with the same average frequency, while the limit cycle solution represents the desynchronized oscillator group which has a frequency distribution in space and appears as to be rotating

with respect to the reference synchronous group. The asymptotic solution of both groups reads

$$\psi = \begin{cases} \sin^{-1}\left(\frac{w_i-\Omega}{\mu R}\right) : |\frac{w_i-\Omega}{\mu R}| < 1 \\ (\tilde{w}_i - \Omega)t + h\big((\tilde{w}_i - \Omega)t\big) : |\frac{w_i-\Omega}{\mu R}| > 1 \end{cases} \tag{1.28}$$

such that $\tilde{w}_i$ is the modified frequency of the desynchronized oscillators given by

$$\tilde{w}_i = \Omega + (\tilde{w}_i - \Omega)\sqrt{1 - \Big(\frac{\mu R}{\tilde{w}_i - \Omega}\Big)^2}. \tag{1.29}$$

and $h(x)$ is a 2π-periodic function. The full solution is given in reference (Sakaguchi and Kuramoto [1986]).

We note that, active rotator Eq. (1.27) is an excitable system. A detailed study of the coupled excitable systems of active rotator type is given in (Bačić [2020]).

1.3 *Summary*

In this chapter we discuss the theory of weakly coupled spiking neural networks, the corresponding phase-reduced model of the weakly coupled neurons and recovery of the Kuramoto model in order to study the collective dynamics of the neural networks. For a network of identical oscillators, the major solution of the system are chimera states emerging as a result of spontaneous symmetry breaking. We conclude the chapter with phase transition phenomenon in the nonidentical oscillators, where the collective fluctuating dynamics is controlled by active rotator equation.

Chapter 2

Pendula Networks

In the previous chapter, the general dynamical behavior of the neurons was discussed and the abstract phase oscillator was introduced as a model for neurodynamic analysis. Notably, such phase oscillator models are obtained using phase-reduction techniques in weakly coupled spiking neural networks. Although it is useful to study the collective dynamics of neural networks, due to their simplicity, first order phase oscillators fail to precisely capture some essential neurodynamics such as coexistence of multiple firing patterns, sensitivity to neuron state and history, and energy dissipation and fluctuations, to name a few. Generally, these lacks are compensated for adding some noise terms to the model.

To this end, one can incorporate these nonlinear effects in a deterministic way by introducing higher orders of phase correction while reducing the neuron model to its corresponding phase-reduction, e.g. augmented phase-reduction discussed in section 1.1. This correction, in turn, increases the degrees of freedom of the phase model.

In this chapter, first we show that such a corrected phase model recovers what is known as the *pendulum* equation, and the detailed dynamical behavior of it are discussed. Moreover, the emerging network behaviors and their mechanisms due to coupling effects are studied for different numbers of pendula in the network and their difference compared to classical chimeras are studied. We end the chapter showing that such chimera states are network attractors that can be engineered for computational purposes.

2.1 *Dynamics of a pendulum* $N = 1$

The equation of motion of a single pendulum reads

$$m\ddot{\phi} + \varepsilon\dot{\phi} + r\sin(\phi) = w. \tag{2.1}$$

where the oscillator parameters m and w are inertia and natural frequency respectively, and ε is the damping ensuring the energy dissipation. The dynamics of a single pendulum consists of a stable equilibrium and a limit cycle. These regimes in the (ε, w) plane inhabit three distinct areas of existence of equilibrium (I), limit cycle (II) and bistability (III) region of coexistence of limit cycle and equilibrium. The bifurcation diagram and dynamical regimes are depicted in Fig. 2.1. In region (I), a single pendulum has two fixed point: a stable equilibrium $O\ (\phi^*, 0)$ and a saddle $S\ (\phi^{**}, 0)$ in the notation$(\phi, \dot{\phi})$. One finds

$$\phi^* = \sin^{-1}(\frac{w}{r}), \tag{2.2}$$

$$\phi^{**} = \pi - \sin^{-1}(\frac{w}{r}). \tag{2.3}$$

Increasing w, the limit cycle is born at curve T_0 also known as Tricomi curve, in a homoclinic bifurcation. In the bistability region (III) the limit cycle and the equilibrium coexist, and can arise due to initial conditions. Further increasing w, the equilibrium is eliminated in an inverse saddle-node bifurcation at $w/r = 1$ and only the limit cycle exists, cf. region (II). We note that, one apparent dynamical difference between the pendulum equation and the active rotator is the appearance of the bistability region for the pendulum, and consequently, the dependence of the dynamics to initial conditions.

In the context of neurodynamics, the pendulum equation acts as an excitable element that starts firing (i.e. spiking) upon receiving external input (or current) exceeding the neuronal threshold. Moreover, the excitability threshold of the pendulum is controlled by parameter r. Decomposing Eq. (2.1) as a system of two first order equations

$$\dot{\phi} = \psi(\phi, \psi), \tag{2.4}$$

$$m\dot{\psi} = -\varepsilon\psi - r\sin(\phi) + w, \tag{2.5}$$

and rearrange it by introducing the translation gauge $\psi \to \psi - w/\varepsilon$, one finds the pendulum equation as

$$\dot{\phi} = \bar{\omega} + \psi(\phi, \psi), \tag{2.6}$$

$$m\dot{\psi} = -\varepsilon\psi - r\sin(\phi), \tag{2.7}$$

where $\bar{\omega} = w/\varepsilon$. This system is identical to the augmented phase-reduction of an active spiking neuron, with the interpretation that the phase parameter

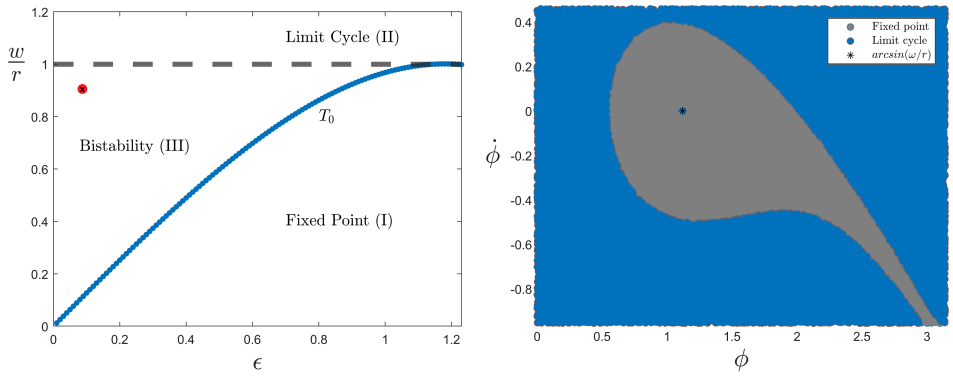

Figure 2.1: Dynamical behavior of a single pendulum consists of a stable equilibrium (fixed point) and a limit cycle. (left) Bifurcation diagram of pendulum dynamics in (ε, w) plane: the limit cycle is born in a Homoclinic bifurcation at Tricomi curve T_0; both limit cycle and equilibrium coexist in the bistability region (III) and dynamics depends on the initial state of the pendulum; equilibrium is eliminated in saddle-node bifurcation at curve $w/r = 1$ and only limit cycle exists. (right) Basins of attraction of pendulum dynamics in the bistability region (III) for a sample point red dot $\varepsilon = 0.1$ and $w = 0.9$. If the pendulum initial states $(\dot{\phi}, \phi)|_{t=0}$ reside in the blue region, the dynamics will fall into the limit cycle attractor, whereas the fixed point attracts the initial states residing in the grey region. The boundary of the fixed point region (grey) is enclosed by the unstable Homoclinic orbit connecting saddle point S to itself, and is tilted due to the presence of damping ε and natural frequency w.

ϕ represents the membrane potential and phase-velocity $\dot{\phi}$ incorporating the variations of the firing rate, the dynamics of each governed by Eqs. (2.6) & (2.7), respectively. In the special case when the firing rate does not include any dynamical variations $\dot{\psi} = 0$, the phase dynamics Eq. (2.6) reduces to one dimensional equation of active rotator type.

The (rotating) limit cycle solution of Eq. (2.1) doesn't have a closed analytical form; an asymptotic solution, however, can be found using perturbation techniques. Decomposing the phase into unperturbed and fluctuating parts $\phi \approx \phi_0 + \lambda\delta\phi$, rescaling time parameter $\tau = \frac{w}{\varepsilon}t$ and introducing small variational parameter $\kappa\lambda = \varepsilon^2/w^2$, pendulum equation reads

$$\begin{aligned} &m\phi_0'' + w\kappa\lambda\phi_0' + r\kappa\lambda\sin(\phi_0) \\ &+m\lambda\delta\phi'' + w\kappa\lambda^2\delta\phi' + r\kappa\lambda^2\delta\phi\cos(\phi_0) = \kappa\lambda w. \end{aligned} \tag{2.8}$$

where $' = \frac{\mathrm{d}}{\mathrm{d}t}$ denotes differentiation with respect to re-scaled time. Sorting for powers of perturbation up to λ^1, one gets the dynamical equations for unperturbed and fluctuating parts

$$\phi_0'' = 0, \tag{2.9}$$

$$m\delta\phi'' + \kappa w\phi_0' + \kappa r\sin(\phi_0) = \kappa w. \tag{2.10}$$

The dynamics of the unperturbed part Eq. (2.9) approximates the pendulum as a phase oscillator with explicit form $\phi_0(t) = \bar{\omega}t + \theta_0$ such that θ_0 is an integration constant interpreted as initial phase. The fluctuating part Eq. (2.10), on the other hand, should be a bounded function. This condition, however, is negated by the presence of the nonsecular term κw acting as an eigenfrequncy. In order to circumvent this issue, we equate the constant velocity with the eigenfrequency, which results in explicit form of the pendulum frequency with respect to pendulum parameters

$$\kappa w\phi_0' = \kappa w \rightarrow \bar{\omega} = \frac{w}{\varepsilon}. \tag{2.11}$$

Inserting these conditions into Eq. (2.10), and replacing the re-scaled time with original form, one gets the fluctuating dynamics

$$\lambda\delta\ddot{\phi} = -\frac{r}{m}\sin(\bar{\omega}t + \theta_0). \tag{2.12}$$

The r.h.s. of Eq. (2.12) depends explicitly on time and one finds the fluctuating dynamics

$$\lambda\delta\phi(t) = \frac{r}{m}\frac{1}{\bar{\omega}^2}\sin(\bar{\omega}t + \theta_0) + \theta_1. \tag{2.13}$$

Then, the final form of asymptotic solution of pendulum up to the first order reads

$$\phi(t) \cong (\bar{\omega}t + \theta_0) + \frac{r}{m}\frac{1}{\bar{\omega}^2}\sin(\bar{\omega}t + \theta_0) + \theta_1. \tag{2.14}$$

The explicit asymptotic approximation of the phase-velocity equation is derived by differentiation of the phase with respect to time

$$\psi = \dot{\phi}(t) \cong \bar{\omega} + \frac{r}{m}\frac{1}{\bar{\omega}}\cos(\bar{\omega}t + \theta_0). \tag{2.15}$$

Notably, the phase-velocity of the pendulum includes variation/fluctuations as a function of the average frequency.

2.2 *System of two coupled pendula* $N = 2$

In the section, we will focus on a system of two coupled pendula and the dynamics that emerges due to the coupling. To that end, we consider a global coupling of sinusoidal form with phase-delay α and coupling strengths fixed at $\mu_{ij} = \mu$ and pendulum parameters $m = 1$, $r = 1$ and $w = 0$ without loss of generality. The equations of motion of the system reads

$$\begin{aligned} \ddot{\phi}_1 + \varepsilon\dot{\phi}_1 + \sin\phi_1 &= \frac{\mu}{2}[\sin(\phi_2 - \phi_1 - \alpha) - \sin(\alpha)], \\ \ddot{\phi}_2 + \varepsilon\dot{\phi}_2 + \sin\phi_2 &= \frac{\mu}{2}[\sin(\phi_1 - \phi_2 - \alpha) - \sin(\alpha)]. \end{aligned} \tag{2.16}$$

similar to the single pendulum case $N = 1$, system 2.16 includes fixed point and limit cycle solutions. In the following, we discuss the details of each solution and possible combinations of solutions emerging due to coupling.

2.2.1 Fixed Points

Let us start by considering the fixed points of system (2.16), obtained by setting $\dot{\phi}_i = 0$ (and consequently $\ddot{\phi}_i = 0$) for $i = 1, 2$. Hence, Eqs. (2.16) reduce to a set of algebraic equations

$$\begin{aligned} \sin\phi_1 &= \frac{\mu}{2}[\sin(\phi_2 - \phi_1 - \alpha) - \sin(\alpha)], \\ \sin\phi_2 &= \frac{\mu}{2}[\sin(\phi_1 - \phi_2 - \alpha) - \sin(\alpha)]. \end{aligned} \tag{2.17}$$

The first set of solutions of (2.17) corresponds to the trivial synchronous fixed points on a $2D$ invariant manifold $\mathfrak{M} = \{\phi_1 = \phi_2; \dot{\phi}_1 = \dot{\phi}_2\}$ such that $\phi_1 = \phi_2 = \phi^o$, with

$$\phi^o = -\sin^{-1}[\mu\sin(\alpha)]. \tag{2.18}$$

We denote this fixed point as O with coordinates $(\phi, \dot{\phi}) = (\phi^o, 0)$ inside manifold $\mathfrak{M}$.

In order to analyze the stability of synchronous fixed points, one needs to find the corresponding Lyapunov exponents (LEs). To that end, we rewrite system (2.16) in the form of first order $4D$ system

$$\begin{aligned}
\dot{\phi}_1 &= \psi_1, \\
\dot{\psi}_1 &= -\varepsilon\psi_1 - \sin(\phi_1) + \frac{\mu}{2}[\sin(\phi_2 - \phi_1 - \alpha) - \sin(\alpha)], \\
\dot{\phi}_2 &= \psi_2, \\
\dot{\psi}_2 &= -\varepsilon\psi_2 - \sin(\phi_2) + \frac{\mu}{2}[\sin(\phi_1 - \phi_2 - \alpha) - \sin(\alpha)],
\end{aligned} \tag{2.19}$$

In the fixed point regime, finding LEs becomes an eigenvalue problem and the LEs are found as roots (denoted by $\lambda's$) of the characteristic equation $|J - \lambda E| = 0$, where J is the system's Jacobian with $J_{ij} = \frac{\partial f_i}{\partial x_j}$. The characteristic equation of system (2.19) reads

$$|J - \lambda E| = \begin{vmatrix} -\lambda & 1 & 0 & 0 \\ -\cos(\phi_1) - \frac{\mu}{2}\cos(\phi_2 - \phi_1 - \alpha) & -\varepsilon - \lambda & \frac{\mu}{2}\cos(\phi_2 - \phi_1 - \alpha) & 0 \\ 0 & 0 & -\lambda & 1 \\ \frac{\mu}{2}\cos(\phi_1 - \phi_2 - \alpha) & 0 & -\cos(\phi_2) - \frac{\mu}{2}\cos(\phi_1 - \phi_2 - \alpha) & -\varepsilon - \lambda \end{vmatrix} \tag{2.20}$$

Using condition (2.18), one finds the trigonometric relations

$$\begin{aligned}
\sin\phi_1 &= \sin\phi_2 = -\mu\sin\alpha, \\
\cos\phi_1 &= \cos\phi_2 = \sqrt{1 - \mu^2\sin^2\alpha}.
\end{aligned} \tag{2.21}$$

Inserting Eqs. (2.21) into the characteristic equation and solving the determinant, one reaches the characteristic equation of system (2.19) in a quadratic form

$$z^2 + 2(\sqrt{1 - \mu^2\sin^2\alpha} + \frac{\mu}{2}\cos\alpha)z + (\sqrt{1 - \mu^2\sin^2\alpha} + \frac{\mu}{2}\cos\alpha)^2 - \frac{\mu^2}{4}\cos^2\alpha = 0, \tag{2.22}$$

where $z = \lambda(\lambda + \varepsilon)$. The l.h.s of Eq. (2.22) can be further simplified into $(z + \sqrt{1 - \mu^2\sin^2\alpha} + \frac{\mu}{2}\cos\alpha)^2 - (\frac{\mu}{2}\cos\alpha)^2$, which gives the final form of the characteristic equation in the form of Vieta's formula as product of the quadratic equations with root coefficients

$$\left(z + \sqrt{1 - \mu^2\sin^2\alpha}\right)\left(z + \sqrt{1 - \mu^2\sin^2\alpha} + \frac{\mu}{2}\cos\alpha\right) = 0. \tag{2.23}$$

Eq. (2.23) has four roots: two LEs $\lambda_{1,2}$ that control the in-manifold stability and $\lambda_{3,4}$ denote the transversal stability of the fixed point inside manifold $\mathfrak{M}$.

The first term of Eq. (1) gives the LE's of fixed point O inside the invariant manifold $\mathfrak{M}$, solving $\lambda(\lambda+\varepsilon)+\sqrt{1-\mu^2\sin^2\alpha}=0$, LE's are found

$$\lambda^o_{1,2}=-\frac{\varepsilon}{2}\pm i\sqrt{\sqrt{1-\mu^2\sin^2\alpha}-(\frac{\varepsilon}{2})^2}. \tag{2.24}$$

The real part of in-manifold LE's are always negative $\Re(\lambda^o_{1,2})=-\frac{\varepsilon}{2}$, indicating that fixed point O is stable. In the region $\mu\sin\alpha<\sqrt{1-\frac{\varepsilon^4}{16}}$, however, $\lambda^o_{1,2}$ are complex valued, therefore fixed point O is a stable focus. Furthermore, point O transforms into stable node at bifurcation curve $\mu\sin\alpha=\sqrt{1-\frac{\varepsilon^2}{16}}$. Above this curve until $\mu\sin\alpha=1$, point O remains a stable node, only to be eliminated in saddle-node bifurcation at $\mu\sin\alpha=1$ (as apparent due to condition (2.18)).

The transversal stability of point O is obtained from second term of Eq. (1). It is straightforward to calculate the LE's $\lambda_{3,4}$ as roots of the equation

$$\lambda(\lambda+\varepsilon)+\sqrt{1-\mu^2\sin^2\alpha}+\mu\cos\alpha=0 \tag{2.25}$$

One finds that the real parts $\Re(\lambda^o_{3,4})=-\frac{\varepsilon}{2}$ are always negative, ensuring the transversal stability of O in the region $\mu\sin\alpha<1$ with $0<\alpha<\frac{\pi}{2}$. Depending on parameter values of (α,μ), transversal stability of O can be in the form of focus or node, depending on $\lambda^o_{3,4}$ acquiring non-zero or zero imaginary part.

The second set of solutions of (2.17) correspond to the fixed point S with coordinates $(\phi,\dot\phi)=(\phi^s,0)$ inside manifold $\mathfrak{M}$, such that

$$\phi^s=\pi-\sin^{-1}[-\mu\sin\alpha], \tag{2.26}$$

which yields the condition

$$\begin{aligned}\sin\phi_1 &= \sin\phi_2=-\mu\sin\alpha,\\ \cos\phi_1 &= \cos\phi_2=-\sqrt{1-\mu^2\sin^2\alpha}.\end{aligned} \tag{2.27}$$

Following same steps as point O, one finds the characteristic equation of LEs of S

$$\left(z-\sqrt{1-\mu^2\sin^2\alpha}\right)\left(z-\sqrt{1-\mu^2\sin^2\alpha}+\frac{\mu}{2}\cos\alpha\right)=0, \tag{2.28}$$

with in-manifold LEs

$$\lambda^s_{1,2}=-\frac{\varepsilon}{2}\pm\sqrt{(\frac{\varepsilon}{2})^2+\sqrt{1-\mu^2\sin^2\alpha}}. \tag{2.29}$$

In the region $\mu \sin\alpha < 1$, $\lambda^s_{1,2}$ are real $\Im(\lambda^s_{1,2}) = 0$ with opposite signs indicating that S is a saddle point. The transversal stability of S is controlled by the remaining LE's

$$\lambda^s_{3,4} = -\frac{\varepsilon}{2} \pm \sqrt{(\frac{\varepsilon}{2})^2 + \sqrt{1-\mu^2\sin^2\alpha} - \mu\cos\alpha}. \tag{2.30}$$

Before S vanishing in saddle-node bifurcation at $\mu\sin\alpha = 1$, $\lambda_{3,4}$ are real-valued as well with opposite signs, hence, point S is also a saddle in transversal direction of the manifold $\mathfrak{M}$.

System (2.17) has two sets of non-trivial solutions outside of the synchronous manifold $\mathfrak{M}$. In order to identify them, first we consider the zero phase-shift $\alpha = 0$ case. Then, the solutions can be identified as $\phi^*_2 = -\phi^*_1$ and $\phi^*_2 = \pi - \phi^*_1$. Inserting these sets into system (2.17) leads to four asynchronous points with coordinate format $(\phi^*_1; \phi^*_2)$

$$N_{1,2} = \quad (\mp\cos^{-1}(\tfrac{1}{\mu}); \pm\cos^{-1}(\tfrac{1}{\mu})) \quad : \phi^*_2 = -\phi^*_1 \tag{2.31}$$

$$N_{3,4} = \quad (\pm\cos^{-1}(\tfrac{1}{\mu}); \pi \mp\cos^{-1}(\tfrac{1}{\mu})) \quad : \phi^*_2 = \pi - \phi^*_1 \tag{2.32}$$

For the case of nonzero phase-shift $\alpha \neq 0$, we use the ansatz

$$\phi^*_1 = \cos^{-1}(-\frac{1}{\mu}) + \alpha, \tag{2.33}$$

$$\phi^*_2 = -\cos^{-1}(-\frac{1}{\mu}) + \alpha, \tag{2.34}$$

for the $N_{1,2}$ asynchronous set. Using the identities

$$\sin[\cos^{-1}(-\frac{1}{\mu}) + \alpha] = \sqrt{1-\frac{1}{\mu^2}}\cos\alpha - \frac{1}{\mu}\sin\alpha, \tag{2.35}$$

$$\sin[-2\cos^{-1}(-\frac{1}{\mu}) - \alpha] = \frac{\mu}{2}\sqrt{1-\frac{1}{\mu^2}}\cos\alpha - \frac{2}{\mu^2}\sin\alpha - \sin\alpha, \tag{2.36}$$

it can be shown that the ansatz satisfies the Eqs. (2.17) and first asynchronous set is obtained. The characteristic equations of $N_{1,2}$ are then obtained by inserting solution set (2.33) into the determinant (2.20)

$$z^2 - (\mu\cos\alpha)z + (1 - \frac{1}{\mu^2}) = 0, \tag{2.37}$$

with $z = \lambda(\lambda+\varepsilon)$. We further simplify the characteristic equation (2.37) into a product of two quadratic forms

$$\Big[\lambda^2 + \varepsilon\lambda - (\eta_1+\eta_2)\Big]\Big[\lambda^2 + \varepsilon\lambda - (\eta_1-\eta_2)\Big] = 0, \tag{2.38}$$

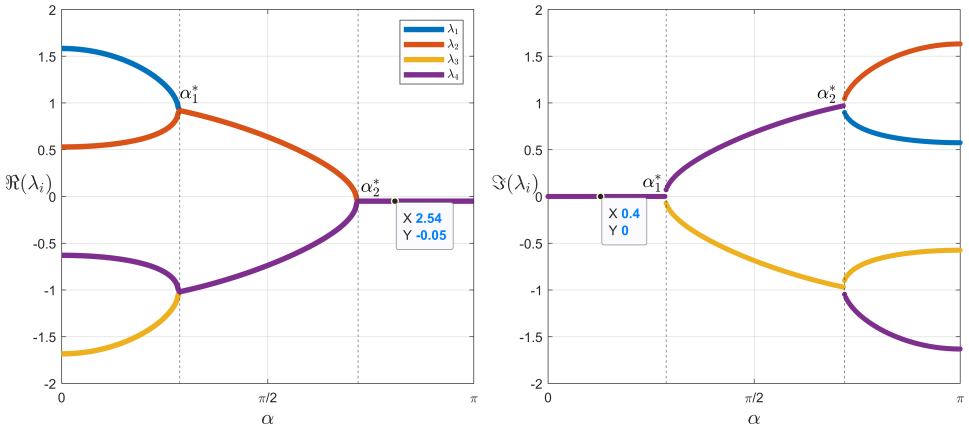

Figure 2.2: The LEs (2.39) of asynchronous fixed points $N_{1,2}$ as a function of α. Other parameters are fixed at $\mu = 3$ and $\varepsilon = 0.1$.

such that $\eta_1 = \frac{\mu}{2}\cos\alpha$ and $\eta_2 = \sqrt{(\frac{\mu}{2} - \frac{1}{\mu})^2 - (\frac{\mu \sin\alpha}{2})^2}$, and the LEs are given

$$\lambda_{1,2} = -\frac{\varepsilon}{2} \pm \sqrt{\frac{\varepsilon^2}{4} + (\eta_1 + \eta_2)}, \tag{2.39}$$

$$\lambda_{3,4} = -\frac{\varepsilon}{2} \pm \sqrt{\frac{\varepsilon^2}{4} + (\eta_1 - \eta_2)}. \tag{2.40}$$

For $\alpha = 0$, first two LEs simplify to $\lambda_{1,2} = -\frac{\varepsilon}{2} \pm \sqrt{\frac{\varepsilon^2}{4} + \frac{1}{\mu}}$; the radical argument is always positive for any $\mu > 0$, hence $\lambda_{1,2}$ are real valued with opposite signs $\lambda_1 > 0$ and $\lambda_2 < 0$. The other LE's read $\lambda_{3,4} = -\frac{\varepsilon}{2} \pm \sqrt{\frac{\varepsilon^2}{4} + (\mu - \frac{1}{\mu})}$; for any $\mu > 1$ $\lambda_{3,4}$ are real valued with opposite sign as well. We conclude that, after their birth at bifurcation curve $\mu = 1$, $N_{1,2}$ are unstable saddle points at $\alpha = 0$. A topological representation would entail that, in the $4D$ space, Ns are attractive in two directions ($\lambda < 0$) and repulsive (unstable) in the other two directions ($\lambda > 0$).

A typical example of LEs for nonzero α and fixed coupling $\mu = 3$ are shown in Fig. 2.6. Increasing α, a first bifurcation happens at $\alpha_1^* = \sin^{-1}(1 - \frac{2}{\mu^2})$, where η_2 has become become purely imaginary, moreover, two of the LEs collide. In this region, Ns become unstable focus-foci. Further increase of α, a second bifurcation happens at $\alpha_2^* \approx \pi - \sin^{-1}(1 - \frac{2}{\mu^2})$. For $\alpha > \alpha_2^*$, η_2 becomes real valued again, η_1, however, is negative since α_2^* is well beyond $\pi/2$. For relatively small values of damping ($\varepsilon < 0.5$), the radical argument is dominated by η_1, and the radical becomes purely imaginary, i.e. $\frac{\varepsilon^2}{4} + (\eta_1 \pm \eta_2) < 0$. In this region, all λ's have negative real part $\Re(\lambda) = -\frac{\varepsilon}{2}$

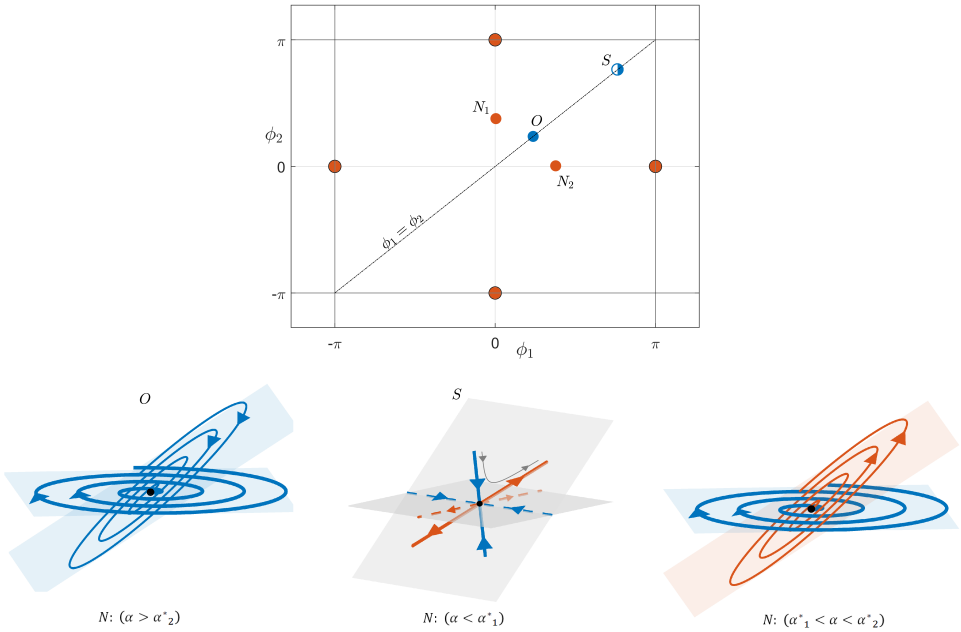

Figure 2.3: (top) Fixed points of the two coupled pendula Eq. (2.16) system. The two points O and S reside inside the synchronous manifold $\mathfrak{M} = \{\phi_1 = \phi_2\}$ while the asynchronous points are outside of $\mathfrak{M}$. Equilibrium O is always stable (focus or node depending on (α, μ)) and S is a saddle. (bottom) illustration of the stability of the fixed points. Blue trajectories denote the stable manifold while red are unstable.

with complex-conjugate imaginary parts, indicating that Ns are stable foci. See Fig. 2.3 for topological illustrations.

The final set of fixed points of system (2.17) are $\{(\pm\pi, 0), (0, \pm\pi)\}$. These points are independent of α and μ and remain unstable.

2.2.2 Limit Cycles

Above the Tricomi curve, the dynamics of a pendulum includes a rotational mode and the system dynamics is consists of two coupled limit cycles. On the synchronous manifold $\mathfrak{M}$, the dynamics of the system Eq. (2.16) reduces to that of one pendulum and both pendula fall into the same limit cycle attractor. The non-trivial limit cycle solutions can be obtained by studying the stability conditions of the synchronous limit cycle and how at its stability border other solutions are born.

In order to study the stability of the synchronous limit cycles, we rewrite

system (2.16) with some non-zero eigenfrequency $w \neq 0$ in new coordinates $x = \frac{1}{2}(\phi_1 + \phi_2)$ and $\delta y = \frac{1}{2}(\phi_1 - \phi_2)$. The equations of motion then read

$$\begin{aligned} \ddot{x} + \varepsilon\dot{x} + \sin(x)\cos(\delta y) &= \tilde{w} - \frac{\mu}{2}\sin(\alpha)\cos(2\delta y), \\ \delta\ddot{y} + \varepsilon\delta\dot{y} + \sin(\delta y)\cos(x) &= -\frac{\mu}{2}\cos(\alpha)\sin(2\delta y). \end{aligned} \tag{2.41}$$

where $\tilde{w} = w - \mu\sin\alpha/2$. First, we study the case of zero phase-shift $\alpha = 0$. System (2.41) reads

$$\ddot{x} + \varepsilon\dot{x} + \cos(\delta y)\sin(x) = w, \tag{2.42}$$

$$\delta\ddot{y} + \varepsilon\delta\dot{y} + \cos(x)\sin(\delta y) = -\frac{\mu}{2}\sin(2\delta y). \tag{2.43}$$

The rotation mode dynamics of the pendula are governed by Eq. (2.42) which can be considered as the general pendulum equation with $r = \cos(\delta y)$. The dynamics of deviation from synchronous limit cycle attractor is explained by self-consistent Eq. (2.43). In order to solve the deviation dynamics Eq. (2.43), we assume small deviations from the synchronous limit cycle $\delta y \ll 1$, hence, Eq.(2.42) is reduced to the standard pendulum equation with rotation solution given by Eq. (2.14) $x \approx (\bar{\omega}t - \theta_0) + \gamma\sin(\bar{\omega}t - \theta_0) + \theta_1$. To this end, stability of the synchronous limit cycle can be rearranged in the form of Mathieu equation

$$\frac{\delta^2 y}{\delta z^2} + (a - 2q\cos 2z)y = 0, \tag{2.44}$$

where

$$a = \frac{4}{\bar{\omega}^2}\Big[\mathrm{J}_1(\gamma)\cos\theta_1 - (\frac{\varepsilon}{2})^2\mu\Big], \tag{2.45}$$

$$q = \frac{4}{\bar{\omega}^2}\Big[(\frac{1}{\gamma} - \mathrm{J}_1(\gamma)\cos\theta_1)^2 + (\mathrm{J}_1'(\gamma)\sin\theta_1)^2\Big]^{1/2} \tag{2.46}$$

$$z = \frac{1}{2}(\bar{\omega}t - \theta_0 + \nu), \tag{2.47}$$

$$y = \delta y\, \mathrm{e}^{-\varepsilon t/2}, \tag{2.48}$$

$$\tan\nu = \gamma\mathrm{J}_1'(\gamma)\tan\theta_1/\mathrm{J}_1(\gamma). \tag{2.49}$$

such that $\mathrm{J_n}$ are Bessel functions of first kind and $\gamma = 1/\bar{\omega}^2$. Moreover, the approximation of the pendulum solution was only taken up to first order; reference [Pedersen et al., 1980] includes full details of the Mathieu equation with higher order terms of pendulum solution. The stability of synchronous limit cycle attractor then translates into the stability of the Mathieu equation. If the system parameters are chosen such that system falls into unstable region, the system undergoes a period-doubling bifurcation in which the synchronous limit cycle switches its stability. The new attractor has a twisted orbit with half the original frequency $\omega_{new} = \frac{\omega_{old}}{2}$ which corresponds to an

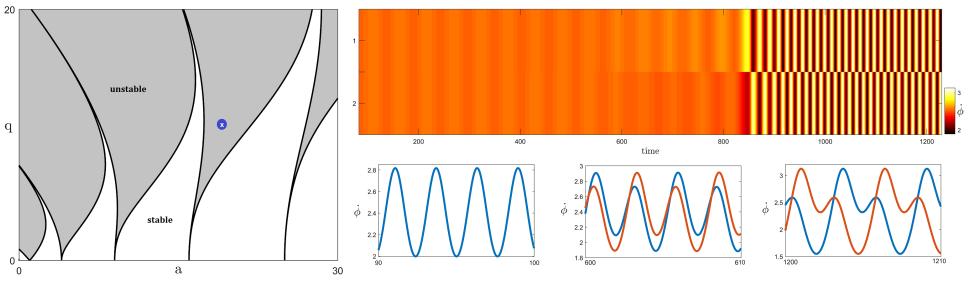

Figure 2.4: Stability of the synchronous limit cycle. (left) The stability diagram of Mathieu equation (2.44). (middle) Velocity time series of the two pendula that reside on the unstable limit cycle attractor, sample point blue dot, with initial deviation $(\delta y, \delta \dot{y}) = (10^{-5}, 0)$. The deviation grows exponentially (right) and the dynamics fall into the stable period doubled limit cycle with two limit cycles locked in anti-phase.

anti-phase locking of the frequencies; this orbit then lies on a $2D$ sheet in $3D$ space, a good visualization of which would be a Möbius band (Fig. 2.5).

An example of the stability regions of Mathieu equation and period-doubling of the limit-cycle is shown in Fig. 2.4. The schematic stability diagram of Mathieu equation in (a, q) plane is shown in Fig. 2.4(left panel); Fig. 2.4 (middle panel) shows how the transient unstable synchronous (rotating) limit cycle evolves/moves into a stable attractor, for system parameters $\mu = 1.4$, $\varepsilon = 0.4$ and $w = 0.97$ with initial condition deviations $(\delta y, \delta \dot{y}) = (10^{-5}, 0)$; Fig. 2.4 (right panel) exponential growth of the initial deviations from unstable limit cycle.

From a physical point of view, the mechanism in which the synchronous limit cycle loses stability is related to the competition between the energy input via the couplings and energy loss due to damping, for a given fixed eigenfrequency. This corresponds only changes in the parameter a of Eq. 2.45 and translates into moving vertically on the Mathieu stability diagram Fig. 2.4 (left). The stability boundary for smaller values of damping, say $\varepsilon = 0.1$, scales in higher values of coupling $\mu \approx |\varepsilon_{old}|^2 \mu_{old} = 22.5$, where $|\varepsilon|$ stands for only the integer value of the damping.

We note that, for the special case $w = 0$, the approximation above doesn't hold and more correction terms need to be taken into account. At large values of coupling strength ($\mu > 22.5$ for $\varepsilon = 0.1$) a synchronous attractor, however, still exists with zero average frequency $\bar{\omega} \sim \langle \dot{\phi} \rangle = 0$ which corresponds to oscillating around origin. If the system falls into unstable region, same period-doubling scenario happens, however, with oscillating limit cycles. For a non-zero phase-shift α, similar scenario holds: for high

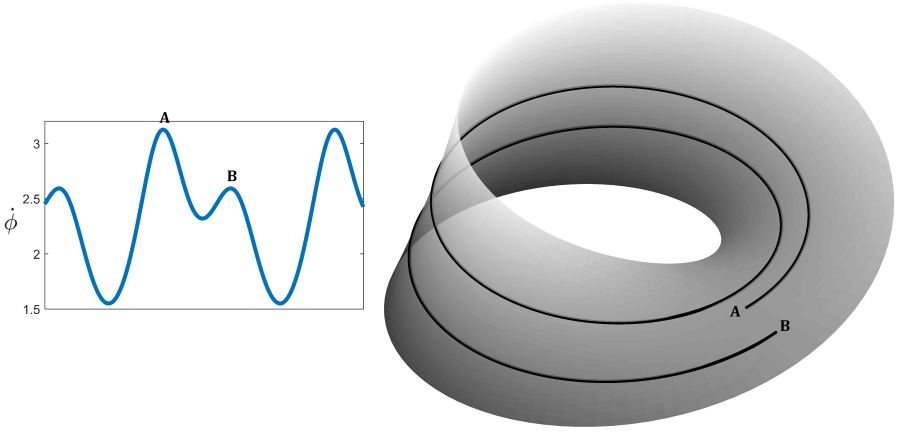

Figure 2.5: A period doubled limit cycle and its topological illustration as a Möbius band.

enough coupling that will push the system to unstable region, a period-doubled limit cycle attractor exists.

The laset set of limit cycle solutions exists as a mixed-mode attractor composed of the limit cycle and a center manifold with an oscillating periodic orbit around a center. The fixed points arising from non-zero α and their unstable manifolds are mostly the core of this mechanism: if the system parameters are chosen such that the pendulum resides in the bistability regime, the dynamics depend on the initial conditions. Then, if the initial conditions of a pendulum falls into the fixed point basins, the dynamics of that pendulum falls into the oscillating center manifold. The approximate solutions of the rotating and oscillating pendula then read

$$\phi = (\bar{\omega}t - \theta_0^{\phi}) + \gamma \sin(\bar{\omega}t - \theta_0^{\phi}) + \theta_1^{\phi}, \tag{2.50}$$

$$\psi = \gamma \sin(\bar{\omega}t - \theta_0^{\psi}) + \theta_1^{\psi}, \tag{2.51}$$

where ϕ stands for the rotating and ψ for the oscillating pendulum. In this case, the oscillating pendulum is driven by the rotating one, hence are frequency locked with a frequency shift $\theta_0^{\phi} - \theta_0^{\psi}$. Moreover, the center coordinate is given by $(\psi, \dot{\psi}) = (\theta_1^{\psi}, 0)$. More details on the mixed- mode attractor, area of existence and basins of attraction will be enclosed in the next section $N = 3$. The exact bifurcation mechanism of the mixed-mode, however, remains for future work.

2.3 $N = 3$ *and Emergence of Chimera States*

The simplest network with non-trivial dynamics can be realized as the minimal network of three pendula with global coupling

$$\begin{aligned}
\ddot{\phi}_1 + \varepsilon\dot{\phi}_1 + \sin\phi_1 &= \frac{\mu}{3}[\sin(\phi_2 - \phi_1 - \alpha) + \sin(\phi_3 - \phi_1 - \alpha) - \sin(\alpha)],\\
\ddot{\phi}_2 + \varepsilon\dot{\phi}_2 + \sin\phi_2 &= \frac{\mu}{3}[\sin(\phi_1 - \phi_2 - \alpha) + \sin(\phi_3 - \phi_2 - \alpha) - \sin(\alpha)],\\
\ddot{\phi}_3 + \varepsilon\dot{\phi}_3 + \sin\phi_3 &= \frac{\mu}{3}[\sin(\phi_1 - \phi_3 - \alpha) + \sin(\phi_2 - \phi_3 - \alpha) - \sin(\alpha)].
\end{aligned} \tag{2.52}$$

Noticeably, such a network has S_3 symmetry. The complex dynamical behavior emerging due to the coupling shall be explored varying parameters $\mu > 0$ and $0 < \alpha < \pi/2$.

Similar to the case $N = 2$, one decomposes system (2.52) into a $6D$ system of first order equations

$$\begin{aligned}
\dot{\phi}_1 &= \psi_1,\\
\dot{\psi}_1 &= -\varepsilon\psi_1 - \sin(\phi_1) + \frac{\mu}{3}[\sin(\phi_2 - \phi_1 - \alpha) + \sin(\phi_3 - \phi_1 - \alpha) - \sin(\alpha)],\\
\dot{\phi}_2 &= \psi_2,\\
\dot{\psi}_2 &= -\varepsilon\psi_2 - \sin(\phi_2) + \frac{\mu}{3}[\sin(\phi_1 - \phi_2 - \alpha) + \sin(\phi_3 - \phi_2 - \alpha) - \sin(\alpha)],\\
\dot{\phi}_3 &= \psi_3,\\
\dot{\psi}_3 &= -\varepsilon\psi_3 - \sin(\phi_3) + \frac{\mu}{3}[\sin(\phi_1 - \phi_3 - \alpha) + \sin(\phi_2 - \phi_3 - \alpha) - \sin(\alpha)].
\end{aligned} \tag{2.53}$$

2.3.1 Fixed Points

System (2.53) has an invariant synchronous manifold $\mathfrak{M} = \{\phi_1 = \phi_2 = \phi_3; \psi_1 = \psi_2 = \psi_3\}$. The in-manifold fixed points of system (2.53) are as before, reading

$$\phi^o = -\sin^{-1}[\mu\sin\alpha],\ \&\ \phi^s = \pi - \sin^{-1}[\mu\sin\alpha]. \tag{2.54}$$

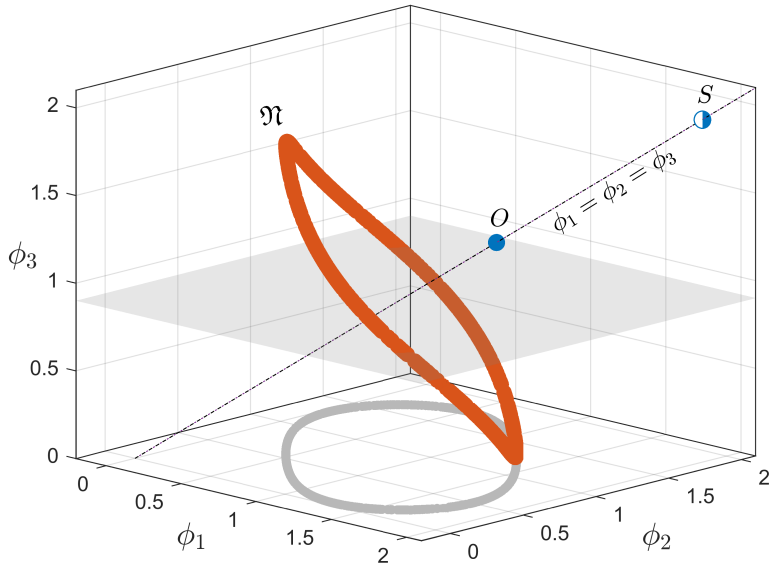

Figure 2.6: Manifold of asynchronous fixed points $\mathfrak{N}$ encircling the synchronous manifold $\mathfrak{M}$. Fixed points of system (2.52) also include a stable equilibrium O and a saddle S inside manifold $\mathfrak{M}$.

The stability of fixed points O and S are obtained via the LEs as eigenvalues of the characteristic equation $|J - \lambda E| =$

$$\begin{vmatrix} -\lambda & 1 & 0 & 0 & 0 & 0 \\ -\cos\phi_1 - \Sigma^1_{2,3} & -\varepsilon-\lambda & \frac{\mu}{3}\cos(\phi_2-\phi_1-\alpha) & 0 & \frac{\mu}{3}\cos(\phi_3-\phi_1-\alpha) & 0 \\ 0 & 0 & -\lambda & 1 & 0 & 0 \\ \frac{\mu}{3}\cos(\phi_1-\phi_2-\alpha) & 0 & -\cos\phi_2 - \Sigma^2_{1,3} & -\varepsilon-\lambda & \frac{\mu}{3}\cos(\phi_3-\phi_1-\alpha) & 0 \\ 0 & 0 & 0 & 0 & -\lambda & 1 \\ \frac{\mu}{3}\cos(\phi_1-\phi_3-\alpha) & 0 & \frac{\mu}{3}\cos(\phi_2-\phi_3-\alpha) & 0 & -\cos\phi_3 - \Sigma^3_{1,2} & -\varepsilon-\lambda \end{vmatrix} = 0, \tag{2.55}$$

where $\Sigma^i_{jk} = \frac{\mu}{3}\big[\cos(\phi_j - \phi_i) + \cos(\phi_k - \phi_i)\big]$. The stability of point O is obtained inserting condition $\phi_1 = \phi_2 = \phi_3 = \phi^o$ into the determinant (2.55), then the characteristic equation reads

$$\left[\lambda^2 + \varepsilon\lambda + \sqrt{1-\mu^2\sin^2\alpha} + \mu\cos\alpha\right]^2 \left[\lambda^2 + \varepsilon\lambda + \sqrt{1-\mu^2\sin^2\alpha}\right] = 0, \tag{2.56}$$

The second term in the l.h.s of Eq. (2.56) gives the two LE's $\lambda_{1,2}$ controlling the in-manifold stability, then O is always stable below curve $\mu\sin\alpha = 1$. Moreover, the first term of Eq. (2.56) controls the transversal stability with the remaining four LE's with multiplicity factor two, i.e. $\lambda_5 = \lambda_3$ and $\lambda_6 = \lambda_4$.

The asynchronous fixed points of system (2.52) emerging after $\mu = 1$ are more complicated: a continuum of unstable points arranged in a $1D$

"ring" type manifold $\mathfrak{N}$ in $3D$ space, encircling the synchronous manifold $\mathfrak{M}$. Fig. 2.6 shows an example of the asynchronous manifold for parameters $\mu = 1.2$ and $\alpha = 0.9$. In a similar fashion to $N = 2$, unstable manifold $\mathfrak{N}$ only stabilizes at some large value of phase-shift $\alpha \approx 2.5$.

The final set of fixed points of system (2.52) satisfies the condition $\phi_i^* = \phi_j^*$ & $\phi_k^* - \phi_i^* = \pi$. Ones finds, contrary to their $N = 2$ counterpart, that these fixed points depend on phase-shift and coupling strength such that $\phi_i^* = \mu \sin \alpha / 3$. Although unstable, they contribute to complicated trajectories of the system in $6D$ space.

2.3.2 Limit Cycles and Chimera States

The synchronous limit cycle for system (2.52) appears in a homoclinic bifurcation and remains stable in the region $0 < \alpha < \pi/2$ until large values of coupling strength $\mu \approx 60$, only to lose stability due to Mathieu equation and turning into a fluctuating period-doubled limit cycle with two [synchronous] pendula locked in anti-phase with respect to the remaining one. Notably, the average frequency $\bar{\omega} = \langle \dot{\phi} \rangle$ of the two components of the new limit cycle attractor are the same, i.e. are on the same Möbius strip. With further increase of μ, however, the two components split into two distinct frequency clusters.

Besides the synchronous-type dynamics arising due to symmetry, counter-intuitive dynamics of "chimeric"-type also emerge in system (2.52). Generally, chimera states refer to spatio-temporal patterns in which a synchronous group of oscillators coexists with incoherent ones. The name chimera, then, stems from the Greek mythological creature with two heads, as if two creatures existing within the same body at the same time.

In the classical Kuramoto model, a chimera state is realized with the bell-shaped frequency distribution of the incoherent group among the uniform synchronous group. In networks of coupled pendula-like oscillators (including Kuramoto with inertia), chimera states manifest as distinguishable clusters with distinct frequencies [Ashwin and Burylko, 2015]. These chimeras reside in large areas of system parameters (α, μ) and have coherent, synchronous in-cluster dynamics. In the region $0 < \alpha < \pi/2$, system (2.52) exhibits three type of chimera states depending on the rotation and oscillation modes of the pendula. In the symbolic notation of average frequencies $(\bar{\omega}_1, \bar{\omega}_2, \bar{\omega}_3)$, we distinguish these chimera states as: $(1 : 2 : 2)$ where all pendula are in rotation mode and one group of pendula $\bar{\omega}_2 = \bar{\omega}_3$ are faster than the $\bar{\omega}_1$; mixed-mode chimera no.1 $(0 : 1 : 1)$ where a pendulum is in oscillation mode $\bar{\omega}_1 = 0$ (center manifold) and the other two are rotating; and mixed-mode no.2 $(0 : 0 : 1)$ in which only one pendula is

rotating and the other two are in oscillation mode.

Fig. 2.7 (left) shows the bifurcation curves and areas of existence of the dynamical behaviors of system (2.52). The synchronous fixed point $O(0:0:0)$ shown in the dotted region, exists from small values of (α, μ) and is stable until saddle-node curve $\mu \sin \alpha = 1$. The synchronous rotation $(1:1:1)$ in the light gray region is born at homoclinic bifurcation curve T_0 and remains stable until Mathieu instability. Notably, the two states $O(0:0:0)$ and $(1:1:1)$ are inside the synchronous manifold $\mathfrak{M}$, hence, T_0 is the equivalent of Tricomi curve in the case of single pendulum, now in different coordinates (α, μ).

Further increase of (α, μ) beyond T_0, the mixed-mode chimera no.1 appears (dark gray region) and remains stable thereafter, coexisting with synchronous rotation state $(1:1:1)$ for the value range shown. The rotation mode chimera state $(1:2:2)$ shown in blue, follows thereafter in a similar fashion and coexists with both mixed-mode no.1 and synchronous rotation states. The mixed- mode no.2 $(0:0:1)$ shown in strips, however, is the last chimera state to appear with increase of (α, μ) and only exists in the striped region. Fig. 2.7 (right) shows the velocity time series in color map alongside the average frequency profiles of the respective behaviors. Note that, below the saddle-node curve $\mu \sin \alpha = 1$ all five behaviors coexist (coincided with striped region), and up to four can coexist above the saddle-node curve. These big areas of coexistence arise due to multistability and emphasize the dependence on initial conditions.

Inside the synchronous manifold $\mathfrak{M}$, the system dynamics reduces to that of one pendulum and dependence on initial conditions is already discussed (see Fig. 2.1 (right)). The phase portrait $(\phi, \dot{\phi})$ of the system inside the manifold $\mathfrak{M}$ is shown in Fig 2.8. After the Tricomi bifurcation curve T_0, there exists a homoclinic orbit connecting the saddle S to itself. If the system initial conditions lie above the homoclinic orbit, dynamic will fall into the equilibrium O, whereas below the homoclinic orbit, the dynamics is a limit cycle. Considering the whole system, the sensitivity to initial conditions becomes more complicated. The network space is $6D$ and multiple unstable and saddle points exits outside of $\mathfrak{M}$ with connecting homoclinic or heteroclinic orbits.

In order to analyze the system behavior with respect to the initial state, however, one can obtain a cross section σ of the $6D$ dynamical space, Fig. 2.9 (left panel). The cross section σ can be obtained by fixing the initial states of two pendula, say no.2 & 3, and varying initial states of pendulum no.1 to obtain the regions of existence (or equivalently basins of attraction) of different system dynamics. Fig. 2.9 (right panel) shows a pixelated cross section σ of the basins of attraction of four system behavior obtained with precision

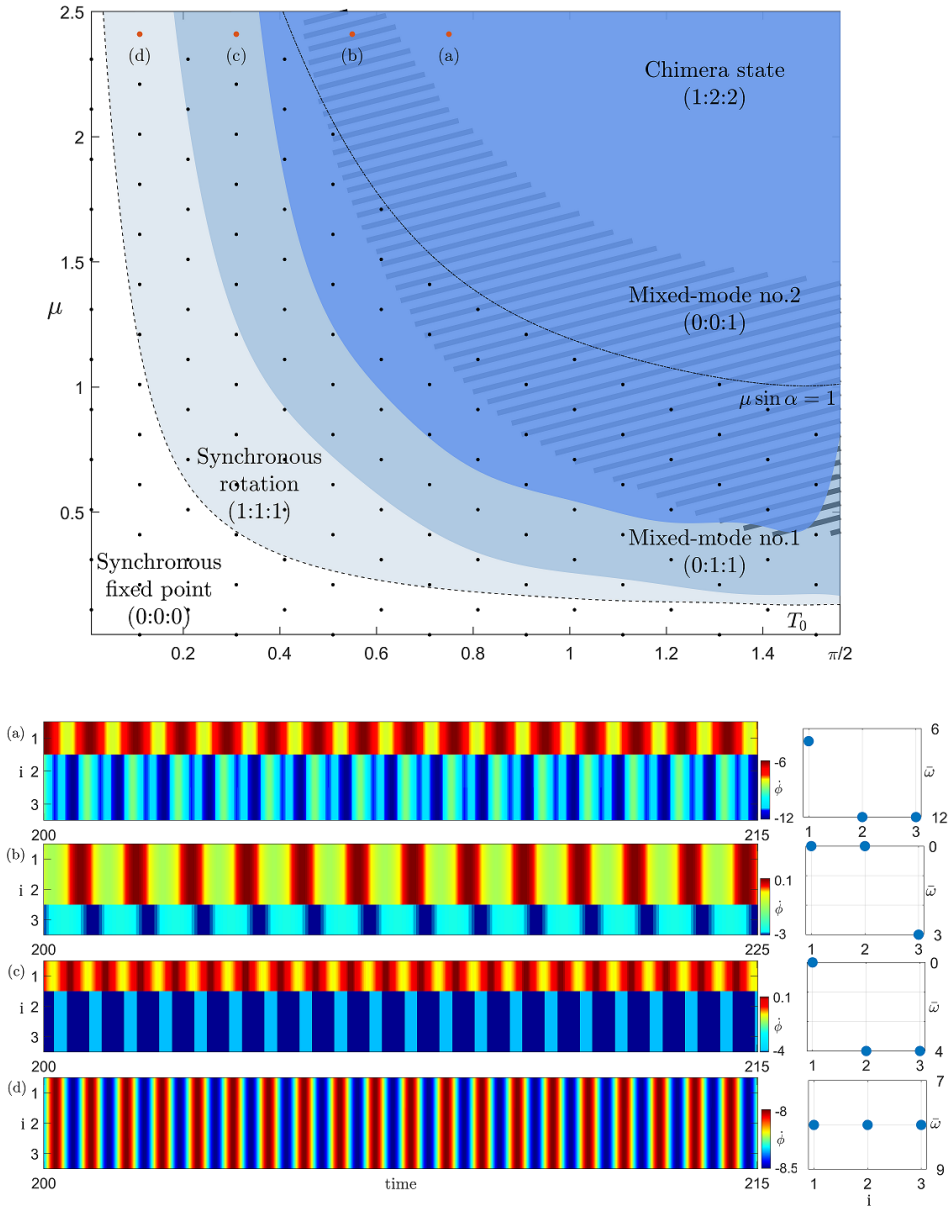

Figure 2.7: The dynamical behaviors of the minimal system of three pendula Eq. 2.52. (top) Bifurcation diagram of the five system dynamics and their regions of existence. Synchronous fixed point (equilibrium) in the dotted region, exists from small values of (α, μ) until elimination in a saddle-node bifurcation at curve $\mu \sin \alpha = 1$. Synchronous rotation state (synchronous limit cycle) in the light gray, is born at Tricomi curve T_0 in a homoclinic bifurcation an remains stable thereafter for large values of (α, μ). (bottom) phase-velocity time series of the dynamical behaviors with the corresponding average frequency profiles for (a) chimera state, (b) mixed-mode no.2, (c) mixed-mode no.1, and (d) synchronous rotation state.

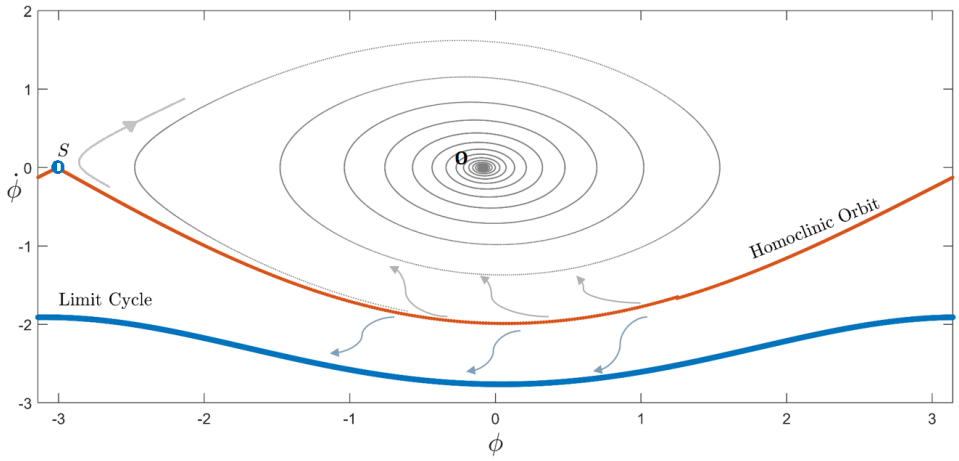

Figure 2.8: Phase portrait of the dynamics inside synchronous manifold $\mathfrak{M}$, after Homoclinic bifurcation. There exists an unstable Homoclinic orbit connecting saddle point S to itself, consequently dividing the dynamics into two regions: if the initial states $(\dot{\phi}, \phi)|_{t=0}$ of the pendulum are above the Homoclinic orbit, dynamics falls into the equilibrium O, whereas below the orbit, the limit cycle attracts the system dynamics.

$h_{\phi,\dot{\phi}} = 0.01$. Each pixel is obtained by solving system (2.52) for $T = 1000$ time units using Runge-Kutta 4th order method with time step precision $\mathrm{d}t = 0.01$, discarding the initial transient time. Different dynamical behaviors occupy different regions of the initial state space (cross section sheet σ) with complex boundary curves separating them. These boundary curves are also known as the separatrix; for the single pendulum case, there exists one separatrix (given that the pendulum parameters are chosen such that the dynamics lies in the bistability region) distinguishing the equilibrium and limit cycle solutions. In the case of $N = 3$ coupled pendula, the separatrixes are more complicated as they are entangled into one an other. The separated regions then represent the basins of attraction of the dynamical behavior.

The basins of attraction of different dynamics and their evolution with respect to phase-shift α are presented in Fig. 2.10 for two different cross section σ's of the $6D$ space: initial states for pendulum no.3 are fixed for both cases, while two different fixed initial states of pendulum no.2 are used in the top and the bottom panel. The basins of attraction then are obtained varying initial values of pendulum no.1 while the coupling strength is fixed at $\mu = 1.2$. The first column in Fig. 2.10 is just below the saddle-node curve, where the equilibrium O occupies big regions (in gray) while the remaining behaviors reside in different areas. With increase of α above the saddle-node curve, equilibrium O is eliminated and the basins of the remaining

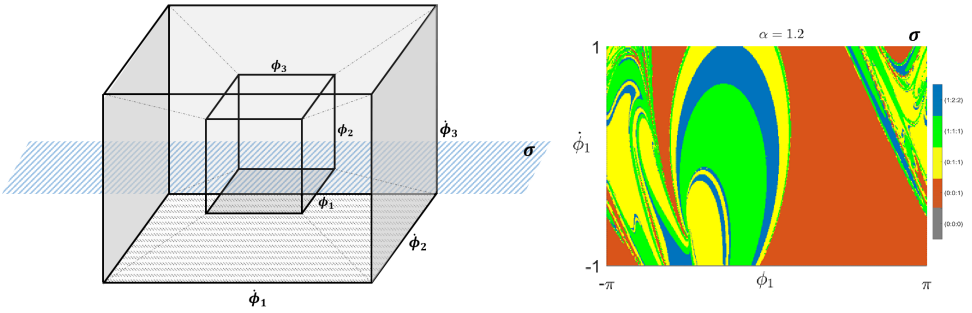

Figure 2.9: (left) schematics of the $6D$ dynamical space of system of three coupled pendula Eq. (2.52), along with a $2D$ cross section plane σ. (right) Basin of attraction of different dynamical behavior (in different colors) residing on the cross section plane σ. See Fig. 2.10 and text for details.

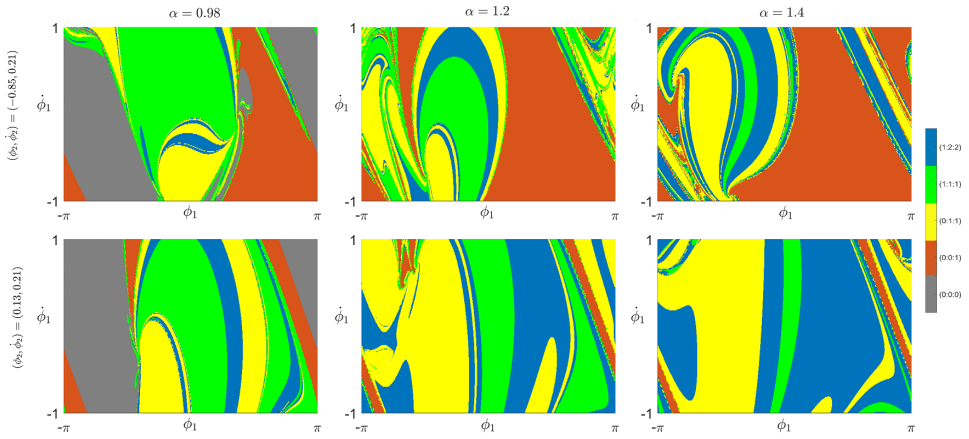

Figure 2.10: Basins of attraction of system dynamics. Two different cross section σ's of the $6D$ dynamical space are shown in top and bottom panels. initial states of pendulum no.3 are fixed for both cases while two different the initial states of pendulum no.2 are chosen. Each cross section is a pixelated plane varying initial states of pendulum no.1 and obtaining the system dynamics by solving Eqs. (2.52) for $T = 1000$ time units with dynamics obtained being color coded. Each dynamical behavior occupies different regions of the cross section sheet and their evolution are obtained for three values of phase-delay α, maintaining coupling strength fixed $\mu = 1.2$.

four behaviors are developed in shape. The striking difference in shape and existence of different behaviors for same values of $(\phi_1, \dot{\phi}_1)$ accentuates the complexity of the system (2.52). More details and implications of the basins of attraction in neural computation will be discussed in chapter 3.

2.4 *Network of Arbitrary Size N*

The equations of motion of a network of N coupled pendula are

$$m\ddot{\phi}_i + \varepsilon\dot{\phi}_i + r\sin(\phi_i) = w + \frac{\mu}{N}\sum_{j=1}^{N}\sin[\phi_j - \phi_i - \alpha], i = 1, ..., N. \tag{2.57}$$

Due to S_N network symmetry (identical oscillators and identical coupling strengths), system (2.57) inherits the synchronous manifold $\mathfrak{M}$ with the synchronous dynamics. The characteristic equation of the fixed points inside the synchronous manifold $\mathfrak{M}$ for a pendula network of arbitrary size N is given by

$$\left[\lambda^2 + \varepsilon\lambda \pm \sqrt{1 - \mu^2\sin^2\alpha} + \mu\cos\alpha\right]^{N-1}\left[\lambda^2 + \varepsilon\lambda \pm \sqrt{1 - \mu^2\sin^2\alpha}\right] = 0. \tag{2.58}$$

such that $+$ corresponds to stable point O and $-$ to saddle point S. It follows from system symmetry that the invariant synchronous manifold always exists for any number N of pendula. The in-manifold dynamics then reduces to the one pendulum equation that recovers the second term of l.h.s of Eq. (2.58). The LEs of transversal stability of $\mathfrak{M}$ are generated by multiplicity from the $\lambda_{3,4}$ of $N = 2$ case.

Corollary: There exists a synchronous manifold $\mathfrak{M}$ for a system of coupled pendula with arbitrary size N which includes two system fixed points: in the region $\mu\sin\alpha < 1$ & $0 < \alpha < \pi/2$, O is a stable focus inside and transversal to $\mathfrak{M}$, whereas S is an N dimensional saddle.

Chimera states solutions of system (2.57), in contrast to their classical counterpart section 1.2, form frequency clusters. Away from secondary bifurcations that destabilizes them, the dynamics of each frequency cluster falls onto a synchronous manifold. Fig. 2.11 shows examples of mixed-mode chimera states with different number of clusters for $N = 100$: (a) two cluster mixed-mode chimera state composed of rotating and oscillating (limit cycle and center manifold) clusters, dynamics of each group is a periodic orbit on the respective synchronous manifolds; (b) with increase of α the mixed-mode chimera develops into three clusters with different average frequencies and their respective orbits develop to higher orders of periodicity; (c)

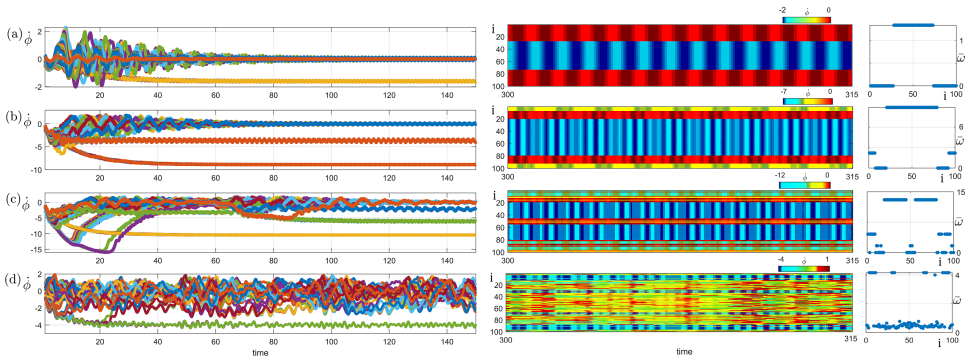

Figure 2.11: Typical examples of mixed-mode chimera state with different number of frequency clusters for system (2.57) of $N = 100$ pendula. Left panel: velocity time plots for $\mu = 2$ and $\alpha = 1.2$(a), 1.35(b), 1.42(c),1.52(d), respectively, and the same fixed initial conditions. Middle panel: sustained frequency profiles of the mixed-mode chimeras (inter-cluster dynamics). Right panel: average frequencies for the individual pendula of the mixed-mode chimeras. Other parameters: $m = 1.0, \varepsilon = 0.1, r = 1, w = 0$.

further increase of α instigates four-cluster mixed-mode chimera state with more complicated orbits; (c) close to a secondary bifurcation near $\pi/2$, the oscillating cluster of the center manifold inherits "fuzzy" orbit while there still exists a limit cycle cluster of rotating pendula. Except for the fuzzy cluster, the inter-cluster dynamics of all the mixed-mode chimeras show synchronous behavior, Fig. 2.11 (middle panel).

The dynamics is then governed on an invariant manifold by the reduced dimension equations

$$\begin{aligned} D(M) = \{&\phi_1 = ... = \phi_{n_1} = \Phi_1(t); ...; \phi_{n_M} = ... = \phi_N = \Phi_M(t); \\ &\dot{\phi}_1 = ... = \dot{\phi}_{n_1} = \dot{\Phi}_1(t); ...; \dot{\phi}_{n_M} = ... = \dot{\phi}_N = \dot{\Phi}_M(t)\} \end{aligned} \tag{2.59}$$

such that the in-manifold dynamics is given by the equations

$$m\ddot{\Phi}_i + \varepsilon\dot{\Phi}_i + r\sin(\Phi_i) = -n_i\tilde{w} + \mu\sum_{j\neq i}^{M} n_j \sin[\Phi_j - \Phi_i - \alpha], \tag{2.60}$$

where $\tilde{w} = \mu\sin(\alpha)$ is the modified eigenfrequency and n_i is the ratio of pendula in the i's cluster to the network size. For different values of parameters (α, μ) and the initial conditions, Eq. (2.60) can develop in different dynamical regions (such as fixed point, limit cycle, invariant torus or chaos).

An analytical approach with asymptotic description can be developed to describe the cluster dynamics. One can represent Φ_i's as sum of a monotonic term with respect to time and correction terms scaled by small perturbation parameter λ

$$\Phi_i = \bar{\omega}_i t + \sum_{l=1}^{\infty} \lambda^l \delta\Phi_i^l \tag{2.61}$$

Inserting condition (2.61) into Eq. (2.60) and sorting by λ, one finds the average frequency of the rotating clusters

$$\bar{\omega}_i = -\frac{n_i \tilde{w}}{\varepsilon} \tag{2.62}$$

and the leading correction term

$$\lambda\delta\Phi_i^1 \sim \frac{r}{m\bar{\omega}_i^2} \sin \bar{\omega}_i t - \mu \sum_{j=1}^{M} \frac{n_j}{\Delta\bar{\omega}_{ji}^2} \sin[\Delta\bar{\omega}_{ji} t - \alpha], \tag{2.63}$$

where $\Delta\bar{\omega}_{ji} = \bar{\omega}_j - \bar{\omega}_i$. The average frequency of the clusters depend on the parameters (α, μ) and the number of pendula in the cluster. The dynamics of each cluster is governed by the interplay of frequency fluctuations of the cluster (first term of Eq. (2.63)) and frequency difference between different clusters (second term of Eq. (2.63)).

From the topological point of view, the dynamics of system (2.57) lies on the surface of a torus $\mathbb{T}^n = \{e^{i\theta_1}, ..., e^{i\theta_n}\}$. The emergence of chimera states identifies the different dynamical clusters as attractors, since each cluster forms a synchronous dynamics and effective dimension of the torus $\mathbb{T}^n$ is reduced. Fig. 2.12 shows the inter-cluster dynamics of two distinct oscillating and highest frequency attractors in three-cluster chimera state with their evolution. After the birth of three-cluster chimera state, each cluster maintains dynamics with high level of periodicity, Fig. 2.12 (top panel). We note that, the representation of periodic motion in this case would be a circle and a sinusoidal curve for oscillating and rotating pendulum, respectively. The degree of periodicity (or quasiperiodicity) could be attained via Lyapunov exponents. Upon increasing either parameter (α, μ) (coupling strength μ in the case of Fig. 2.12) the complexity level of periodicity increases for the cluster dynamics (Fig. 2.12 (bottom panel)) before the chimera state loses stability, initiating the birth of a different chimera state. We emphasize that, the complexity of the inter-cluster dynamics are better reflected in the phase-velocity variations rather than the phase, as the variations of the phase parameter of all pendula are scaled by the average cluster frequency $\frac{1}{\bar{\omega}^2}$, which reduces to $\frac{1}{\bar{\omega}}$ for the phase-velocity upon differentiating.

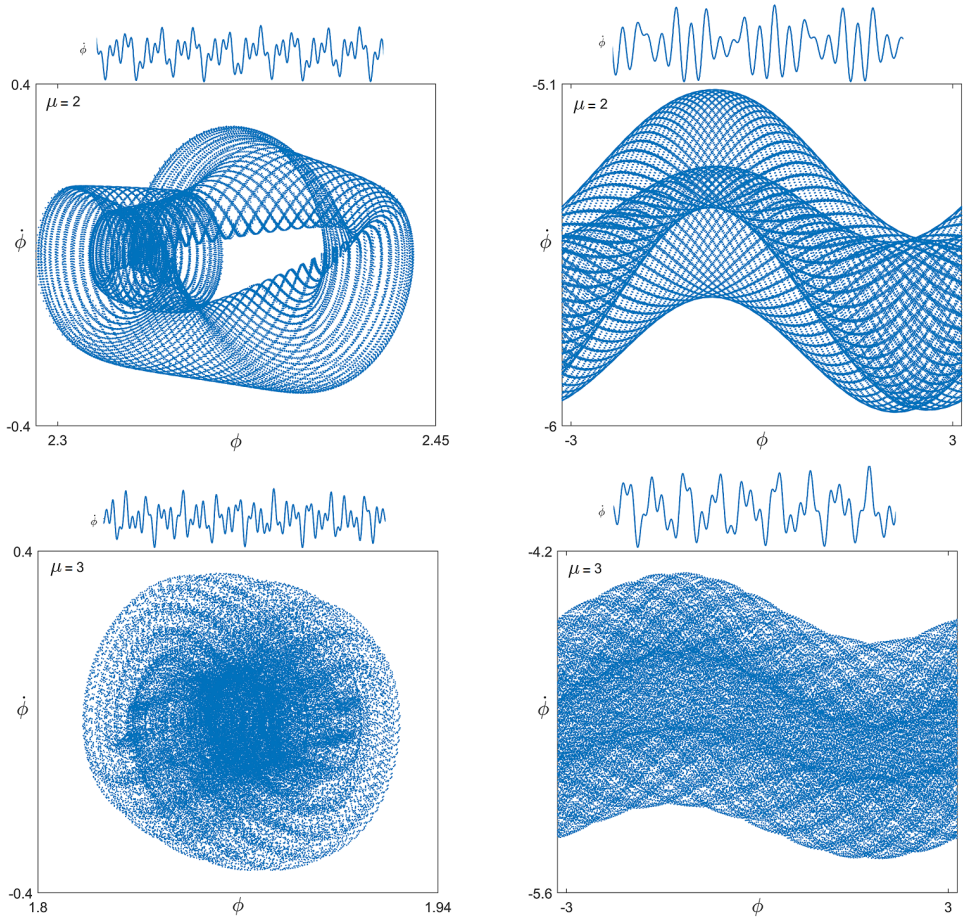

Figure 2.12: Evolution of the inter-cluster dynamics of two different clusters in the three-cluster mixed-mode chimera state with regards to coupling strength μ. (top panel) At $\mu = 2$, the dynamics of the center manifold and the next neighboring rotating cluster (left and right, respectively) include higher orders of periodicity as a result of intra-cluster coupling effects Eq. (2.63). (bottom panel) the complexity of the periodicity develops with increase of coupling strength μ. The phase-delay parameter is fixed for both cases $\alpha = 1.4$.

2.5 *Summary*

In this chapter we analyzed the dynamical behavior of networks of coupled pendula for various network sizes. The pendulum equation is shown to be a similar to the augmented phase-reduced model of a spiking neuron. The fluctuations of the phase-velocity of the pendula are captured by a damping coefficient ensuring energy dissipation and a nonlinear sinusoidal term arising due to gravitation. In the context of neurodynamics, these coefficients can be understood as neuron's interaction with the environment (thermal or otherwise) and excitability mechanism.

The nontrivial counter-intuitive dynamics of a pendula network includes mixed-mode chimera states manifested as distinct frequency clusters. Paradoxically, and in contrast to their classical counterparts, the mixed-mode chimera states show higher level of order in presence of energy dissipation. The stability and existence regimes of the different mixed mode-chimeras are identified for the minimal network of $N = 3$ pendula in the (α, μ) plane where α is the phase-shift and μ the coupling strength. Due to the multistability, almost all dynamical behaviors can coexist in some strip regions of (α, μ) parameter plane, the rise of each solution then depends highly on the initial states of the pendula.

The large coexistence regions of different solutions establishes the idea of network of attractors with each chimera state (and synchronous states) as an attractor in the network space that are connected to one an other. The basins of attraction and dependence to the initial states are obtained showing complex separatrix curves distinguishing between different solutions. The exact mechanism in which these separatrixes arise remains for future studies.

We conclude the chapter with qualitative study of the cluster dynamics for a network of arbitrary finite size. The topological properties of the attractors and their clusters such as their dimension remains for future studies.

Chapter 3

Attractor Networks and Neural Computation

In dissipative systems, there exist attracting sets such that the system trajectory progress towards. In networks of coupled dynamical elements such as coupled oscillators or neurons, such attracting sets are called *attractor states*, or simply attractors, with their emergence and stability condition depending on the coupling parameters (Auslander et al. [1964]). After the success of Hopfiled networks explaining the associative memory as attractor states in neural networks (Hopfield [1982]), there has been numerous studies on the role of sustained neural activity as attractor states for cognitive tasks and working memory (Compte [2006], Khona and Fiete [2022]).

In chapter 2, we discussed the existence and emergence mechanisms of attractor states in network of coupled pendula as mixed-mode chimera states. In contrast to the classical chimera states, such chimera states may coexist for the same set of system parameters near each other in the network space, such that the system trajectory depends on the initial conditions. Note that, in standard Kuramoto model, chimeras coexist with stable equilibrium (fixed point).

In this chapter, first we review how the attractors are considered as computational components in some aspects of brain functionality and bio-inspired computing schemes, such as reservoir computing. we investigate how the system multistability establishes the network of chimera states, concluding the chapter with qualitative study on the landscape of such attractor network.

3.1 *Introduction*

The study of the brain has been [directly or indirectly] one of the challenging areas for natural sciences, psychology and philosophy throughout the human history. In the realm of philosophy, it dates back to the works and interests of Aristotle (384-322 BC) where the relation between inner workings of mind and how they affect the human experience was considered. During the 15th century, the word *cognition* was forged, referring to the mental action or process of acquiring knowledge and understanding through thought, experience, and the senses. However, it was only in the Enlightenment era that groundwork for modern concepts of cognition was developed. One of the most interesting philosophical works during the German idealism is Hegel's *philosophy of mind* [Hegel and Inwood, 2007], where Hegel, to roughly put it, distinguishes between the physical organ responsible for the thoughts and its virtual embodiment as "logical space of reason", or the mind, which is populated by meaningless words that coexist in juxtaposition to each other therein; in other words, thought process' occur.

During the 1990's, the development of cognitive science (predominantly psychology based) presented theories highlighting the necessity of cognitive action as embodied, extended, and producing dynamic processes in the mind.
Nowadays, it is generally considered that cognitive process' span all aspects of intellectual functions such as perception, thought, formation of knowledge, memory, decision making, computation etc.

An example of a cognitive process can be understood as generalization of a concept, say tree, to extract the important properties of the concept "tree" from various objects "tree" in order to simplify and store it. This process enables for high-level thinking, as the subject (e.g. human) needs not to store all the information about all the trees used to learn the concept tree.

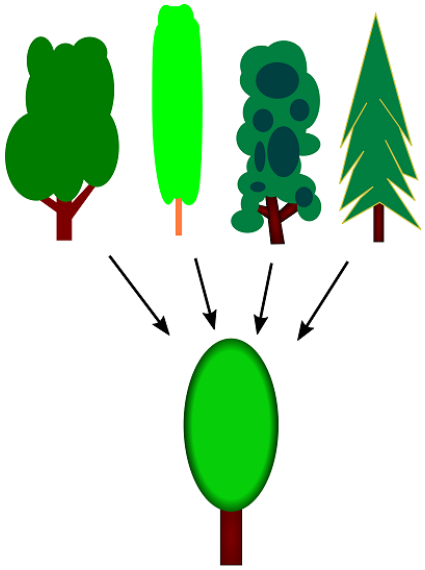

Figure 3.1: Cognitive simplification of a concept "tree" for abstract thinking.

The distinction, as Hegel suggested, between physical organ (the brain) and its virtual realization in the logical space (the mind) allows for the following question: what is the relation between the

electrochemical reactions in the brain and the thought process' in the mind? How can one affect the other? In order to be able to formulate these questions rigorously suitable for natural science, one can alternate these questions to the following: what are the computational abilities of a neural network?

At the dawn of modern technological advances, the idea of building computing devices was bearing fruit. Majority of crucial ideas of computers was developed by Alan Turing and John von Neumann. Since the brain is considered to be the main computing component of the central nervous system, some early ideas for a computer were drawn from the brain. An illustrative example of such ideas are discussed in lectures notes of von Neumann "The Computer And The Brain". As von Neumann argues, the two critical aspects of a computing device (including the brain) are the form of "computation" and "memory". Of course, computing devices already existed for millennia (simple calculators) and using apparatus for Arithmetic was known. Hence, the "computation" aspect for a modern computer was introduced as the bit system. The "memory" aspect, then, was taken care with the introduction of von Neumann architecture, to simplify it, separated the computation center from the memory center, with memory center including all the information, or "memory items". In practice, the von Neumann architecture of the separated memory and computation units poses serious problems, in the big data simulations for example.

A closer look into the brain, however, reveals that there does not exist a separate storage center in the brain, it is integrated with the computation part. In this sense, memory is entirely not equivalent to storage, as is in the computer. Several scenarios for manifestation of the memory suggest that, for example, the variations of the stimulation criteria (i.e. threshold) with time as a function of neuron's previous state may account for memory. This scenario revolves generally around the neuron models and responses to stimuli. Another embodiment of the brain memory suggests the variations of the connections, or synapses, over time. In this scenario, which is now known as synaptic plasticity, the stimulation criterion for synapses may change according to activity over the synapse.

3.1.1 Associative memory

In 1982, J. Hopfield suggested that, neural networks as a form of dynamical systems can inherit *associative memory* through their emergent collective behavior. In Hopfield neural networks, a memory unit can be realized as a stable fixed point of the system. Let $x = (x_1, ..., x_n)$ be the coordinates of the system that has locally stable fixed points $x_a, x_b, ...$, with each one assuming

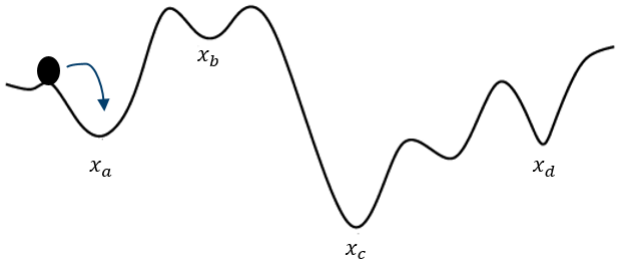

Figure 3.2: Fixed points of a Hopfield neural network represented as local minima that encode associative memory. Upon receiving some information about the memory (the ball) system dynamics approach the respective fixed point and the memory unit is retrieved

a basin of attraction. The information can then be stored in the system's fixed points as the content-addressable memory, since each fixed point x_a represents a perfect knowledge about the stored information and can be retrieved even with a partial knowledge (or deformation) $x_a + \delta$ of the details of the information unit, as long as the deformation lies in the basins of attraction. The retrieval process occurs as the system coordinates proceed in time until $x \approx x_a$.

The computation procedure of a real modern computer can be regarded similar to the mechanism of the Hopfield system. In a digital computer, for example, the data are stored as binary registers (fixed points), upon receiving input the computer starts to update its state with the clock ticks, following a rule that is built in by design of the machine. After a while, computer stops the change of its state and the computation has been reached. In this sense, a digital computer is a digital discrete dynamical system of Hopfield type with its fixed points having a physical realization, the memory storage.

The associative memory, although illustrative for analyzing the system behavior, is limited for real world computational purposes. In order, for example, to store a 10 bit data there needs to be 1024 attractors. One method for overcoming this issue is to devise a "dynamic" associative memory, where the sequence of the attractors carries the means of computation: the discrete sequential information transforms complex cognitive brain activity into a low-dimensional dynamical process. The basic idea for a system inhabiting sequential dynamics is to annihilate the [stable] fixed points, leaving only the saddle points. The network of saddles are connected via Heteroclinic orbits and due to their unstable nature, system will always jump from one saddle point to another, mimicking limit cycle behavior equivalent to spiking of the neurons [Rabinovich et al., 2020].

In order to better demonstrate the dynamical regimes of a system and

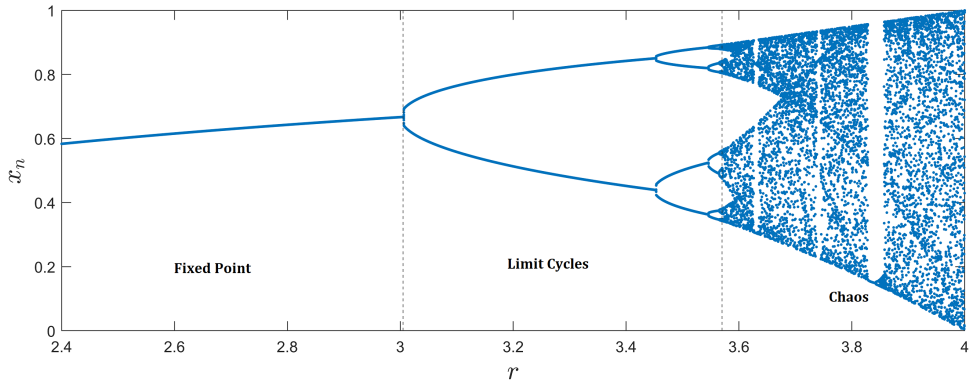

Figure 3.3: Dynamical regimes of logistic map includes fixed point, limit cycle (including period-2, period-4 and period-8 orbits) and chaos.

their meaning for computation, we can analyze the simple example of logistic map

$$x_{n+1} = r x_n (1 - x_n), \tag{3.1}$$

where x is the state updated according its previous states. The dynamical regimes are established varying the parameter r, Fig. 3.4. For small values of $0 < r < 1$ system (3.1) assumes the fixed point regime, with the fixed point existing at the origin that attracts all the initial values; at $r = 1$ the fixed point in the origin becomes unstable, giving rise to stable fixed point outside of origin at the interval $1 < r < 3$. The limit cycle dynamical regime emerges for $3 < r < 3.569$ such that state x_n approaches a permanent oscillation between 2^m, $m = 1, 2, 3, ...$ fixed values, consequently a limit cycle has emerged. The chaos dynamical regime appears at $r > 3.569$: the chaos is a Cantor set at values of $r \in [3.569, 4]$ existing with periodic windows of large periods which are dense at $r \in [3.569, 4]$. Furthermore, the chaotic dynamic can be understood as any slight change in the initial conditions will result in dramatic final states of x_n.

The Hopfield network then operates in the fixed point regime of its dynamical properties, while a Heteroclinic attractor network is attempted to push the system to function in the limit cycle regime.

3.1.2 Physical Realization of NNs and Reservoir Computing

In previous section the idea of distinction between the brain and its virtual realization that allows for computation (mind) was introduced and computational abilities of neural networks were analyzed. The concept of associative memory (and its variations) opens the door for understanding how can

data be stored in a neural network without the need for a separate storage unit, as is in the brain, hence how the "mind" relates to the "brain". Computation then can be understood as combination of such memories under a certain law in order to produce results (binary process in the computer). Now one can as the question: what are the perquisites for a physical system to inherit memory? Initially, one needs to dissociated from the usual understating of the word memory almost entirely used as engravings of the events, pictures, or generally some sort of data in the human brain. A thorough description of a memory, ironically a poetic interpretation as well, is "traces of the past": the present state of a physical system (footsteps in the sand, water surface waves of a pond, etc.) reveals information about that system's past states.

This fact can be best illustrated in C. Rovelli's thought experiment [Rovelli, 2022]: a system of small balls moving freely in a confined room without energy loss, having elastic collisions, and some pendula hanging from the ceiling of the room. The pendula naturally have energy dissipation and oscillations of pendula are damped, hence one can safely assume the state of the pendula at rest, maybe with some small thermal fluctuations. The event of collision between a ball and a pendulum results in energy transfer from the ball into the pendulum, hence pendulum can start damped oscillation. The oscillating motion of the pendula observed at a given time then, are analogs of memory, revealing about the events/collisions of the past. One can assign thermal energy function to the ball and pendula system that defines a temperature: $E_i = \frac{1}{2}k_B T_i,\ i = e, m$, such that e and m stand for environment and memory systems, respectively. Since the collision process is irreversible, the ball environment and pendula system cannot be in thermal equilibrium, with each event increasing the entropy of the total system $\Delta S \sim \frac{\Delta E}{T_m} - \frac{\Delta E}{T_e}$. Then, the first necessary condition for inheritance of memory is *low entropy* ($T_e > T_m$). Other necessary condition is relative long relaxation (or thermalization) time τ_m of the memory system compared to the transient time for lasting of the memory. This can be realized by weak coupling between the pendula, as the energy can diffuse via the couplings back and forth. To summarize, a dynamical [physical] system is capable of inhibiting memory if it satisfies these conditions: Separation of the memory system from an environment that would provide information, thermodynamical imbalance which allows for the energy flow and information transfer, and long thermalization/relaxation of the memory system which is provided by weak coupling in the memory system.

Reservoir computing emerged as a paradigm shift for training of the recurrent neural networks (RNN). The main idea of reservoir computing (and RNNs in general) consists of mapping of the input data into a high-dimensional space in which the necessary information can be obtained easily by a linear reading. It was proposed that, instead of training all the con-

nections in a RNN structure, it suffices to implement the learning algorithm only on the output layer, under certain condition, due to the linearization of the data in the output layer. The benefits of this method is that, although losing some performance accuracy, any substrate can be used as the computational medium (reservoir) with lesser training costs, e.g. energy and time. Although reservoir computing is being used as an umbrella term covering the growing methods in the field, two main branches are worth mentioning.

Liquid-state machine (LSM) in which the reservoir is an excitable medium that, in contrast to attractor networks, has only one attractor, the ground state. The means of computation then, are transient patterns that are created by means of perturbation (i.e. input data), each point in time-space of the transient state representing the present and the past history of the input. It is essential then, that hte reservoir dynamics should not be chaotic. This method is closer to biological neural networks, as the reservoir can be constructed of spiking neurons, and different transient states are created by the rapidly changing temporal inputs. It is however, difficult to implement LSM for practical purposes, since for example, there is the need for the fine-tuning of the temporal resolution of the transient states with regard to unknown input. Moreover, non-chaotic elements may construct chaotic collective dynamics, or in presence of periodic forcing (Duffing oscillator for example).

Echo-state network (ESN) in which the reservoir is considered as a black box with its dynamics not of immediate concern. The network elements consist of neuron models representing a statistical view of the firing rate of spiking neurons, e.g. sigmoid neurons. The network connectivity is fixed, usually generated at random with a certain connectivity distribution that ensures the *echo state property*: the network's memory of the initial state or perturbations fades in time. It is shown that, the spectral radius of the connectivity matrix smaller than 1 ensures the echo state property for the sigmoidal neurons [with leak]. Although easier to implement for practical purposes, the dynamical behavior of the ESNs do not represent biological systems and there is no exact recipe for initializing the network structure or its states. One can only check if the network structure satisfies the echo state property, and manually find a fine tuning for the network size with respect to the task at hand.

It is evident that the general methods of reservoir computing follow Rovelli's memory conditions of a physical realization of a system inheriting memory.

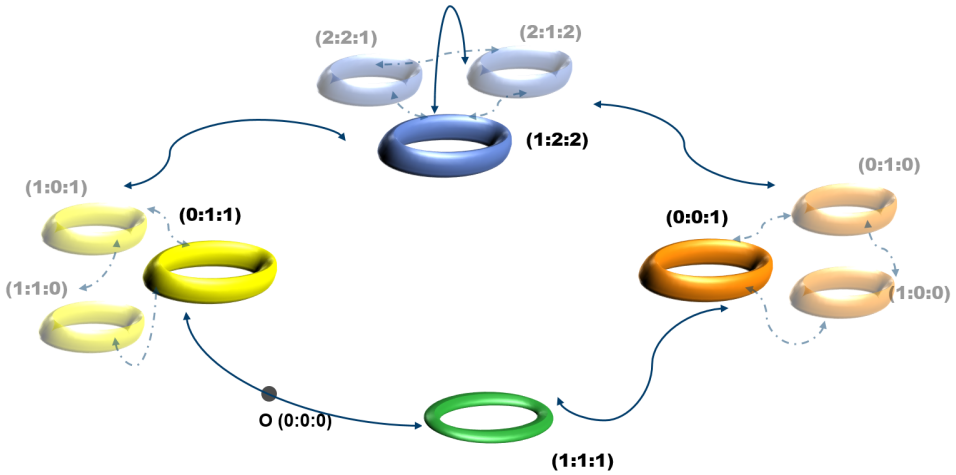

Figure 3.4: Sketch of attractor network of the minimal system $N = 3$ of coupled pendula Eq. (2.52).

3.2 *Chimera Networks*

In order to construct a computing system that inherits memory and enables for computation, one also needs to know the exact dynamics of the system in question, one fact that was mostly overlooked in reservoir computing methods. The computation principals then will follow naturally thereafter. In chapter 2 we analyzed the intrinsic dynamics of pendula networks. Three dynamical regimes consisting of fixed points, limit cycles and chaos-like were identified for networks of any finite size $N > 3$. It was shown that, the system can be tuned into each of these regimes by two parameters: phase-shift α and coupling strength μ. The fixed points are found at the edges of the phase-shift domain $\alpha \in [0\ \pi]$. In the limit cycle regime, chimera states emerge and manifest as frequency clusters. The nature of these frequency cluster chimera states are different than their classical counterparts: they are not "chaotic transient" and coexist in large areas of the parameter plane (α, μ) as attractor states. The chaos in this system can be understood as extreme sensitivity to the initial conditions. The system's trajectory then can arbitrarily visit the different attractors with infinitesimal change in the initial conditions. In non-chaotic region ($\alpha < \pi/2$) system dynamics is not extremely sensitive to initial conditions, with each attractor inheriting regions for the basins of attraction. In other words, if the initial conditions of the system (or perturbations) span the basins of attraction of a certain attractor, system dynamics will approach it.

For the minimal system size $N = 3$ there exists three types of distinct

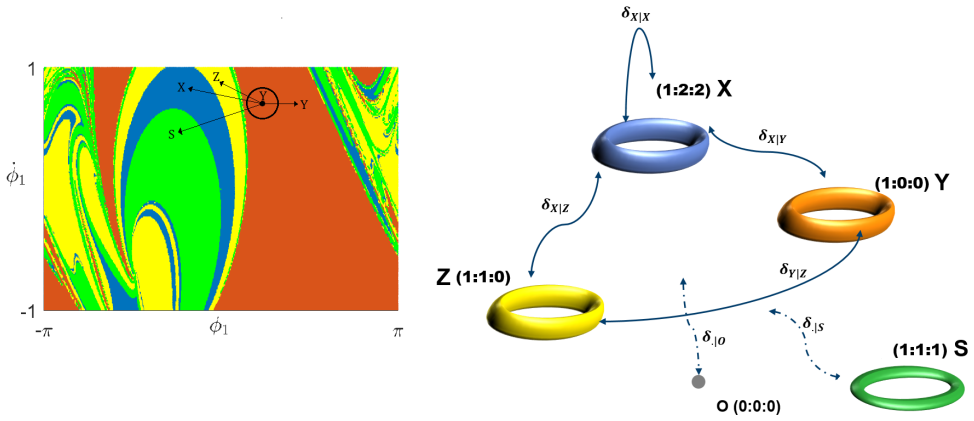

Figure 3.5: An attractor network is formed via coexistence of chimera states due to multistability of the coupled pendula-like objects for minimal system of $N = 3$ with three symbols X, Y, and Z are assigned to each chimera type, with S representing the synchronous rotating state and O as the synchronous fixed point, for brevity. (left) cross section sheet σ of the initial state space showing the basins of attraction of the dynamical behaviors at system parameters $\alpha = 1.2$ and $\mu = 1.2$ (adopted from Fig. 2.10). (right) Sketch of the attractor network consisting of chimeras (colored $\mathbb{T}^2$ tori) and synchronous rotation and fixed point states. The connections between the attractors are denoted by $\delta_{.|.}$. The value of $|\delta_{.|.}|$ represents the transition probability between the attractors and corresponds to the area of the basins of attraction of each attractor to the total area of the cross section.

chimera states, with three replicas of each chimera due to permutation symmetry of the system. From the topological point of view, coexistence entails that the attractors are connected to each other in the dynamical space. Fig 3.4 shows a schematic of the attractor network in the dynamical space; each chimera is represented by a colored $\mathbb{T}^2$ torus with their replica in fade, the synchronous rotation state with an invariant circle $S(1:1:1)$ and the synchronous fixed point with $O(0:0:0)$. We will refer to this ensemble of behaviors in the dynamical system as chimera network. In the following, we qualitatively consider the dynamical and topological properties of this type chimera network.

The connections between the attractors can be understood as transition probability $\delta_{i|j}$ between the attractors i and j. The value of transition probabilities $\delta_{i|j}$ can roughly be represented by the area of the basins of attraction, Fig. 3.5. Moreover, the separatrices (and consequently the area of the basins) depend on the phase-shift α, recall Fig 2.10. The connectivity $\delta_{.|.}$ between the chimeras then depends on the phase-shift and can be tuned.

In the region $\alpha < \pi/2$, the basins of attraction are large and chimeras do not switch spontaneously. In order to switch between the attractors, there needs to be an input in the form of a perturbation, schemed as the arrows in Fig. 3.5 (left). An attractor network can be excitable (Ceni et al. [2020]), such that there exists a threshold for perturbation magnitude. A perturbation with magnitude above the threshold may results in a switch. Moreover, the switching pathway is via the unstable manifold of saddles; the perturbation direction is equally important as the magnitude, if the direction enables the trajectory towards the saddle. The magnitude of the smallest perturbation that results in switching between chimeras is defined as the threshold $\delta = 0.001$, Fig 3.6. The connection between the chimera states is excitable. Here we only measure the probability of a switch p, without distinguishing the chimera that the system switches to.

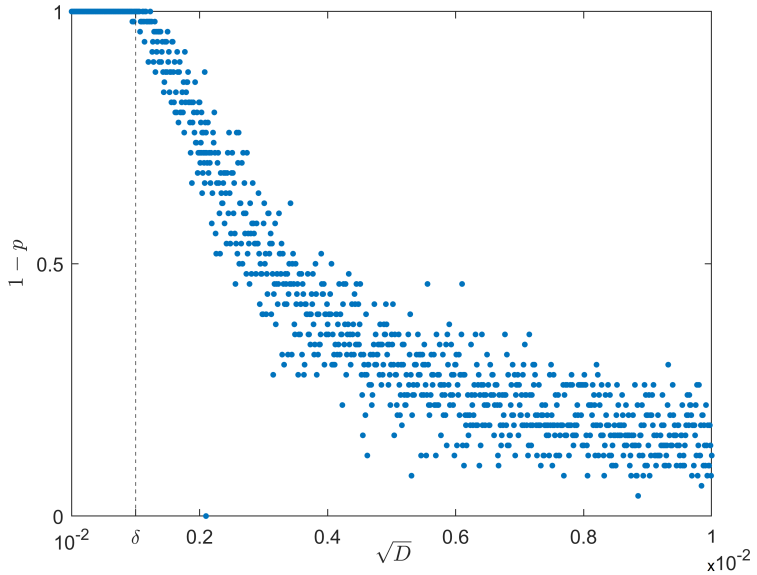

Figure 3.6: Excitability of the $(1:2:2)$ chimera state in presence of white Gaussian noise of intensity $\sqrt{D}$ and the relative threshold δ at system parameters $(\alpha, \mu) = (1.4, 1.2)$. At small noise intensity system (2.52) does not switch, after the threshold δ, the switching probability p was calculated for 100 iterations.

For $\alpha > \pi/2$, however, chimera states change stability becoming saddles and spontaneous switching between chimera states takes place. Hence, the connections between chimera states are interpreted heteroclinic [Goldschmidt et al., 2019, Zhang et al., 2020, Brezetsky et al., 2021b]. The exact relation between the connectivity $\delta_{||}$ and α and the mechanism in which the chimeras change stability remains for future work.

For the minimal $N = 3$ case, three symbols X, Y, and Z are assigned to each chimera type, with S representing the synchronous rotating state

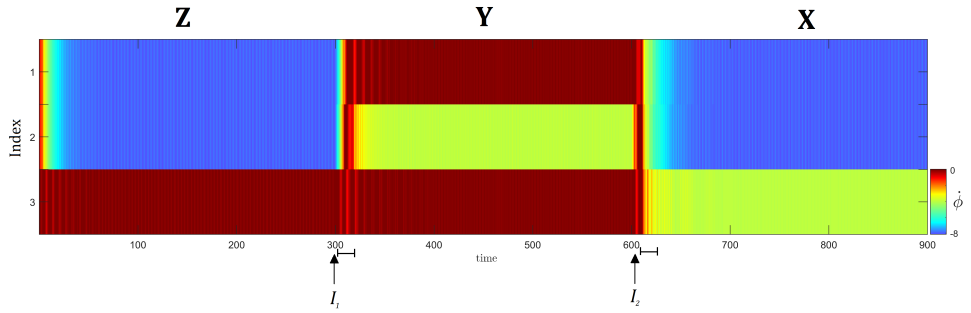

Figure 3.7: Input-driven switchings between chimera states. Three different chimera states are label such that $X: \ (1:2:2), Y: \ (1:0:0), Z: \ (1:1:0)$.

and O as the synchronous fixed point. Fig. 3.7 shows the sequence $Z \rightarrow Y \rightarrow X$ of two switches between three chimera states invoked by two short-lived perturbations I. Each $I = (\delta\phi_1, \delta\phi_2, \delta\phi_3)$ includes phase perturbations such that $I_1 = (0.6, 0.8, 0.9)$ and $I_2 = (0.1, 0.8, 0.6)$ and null components in transversal direction to the limit cycle, i.e. $\delta\dot{\phi}_i = 0$. Moreover, coupling parameters $(\alpha, \mu) = (1.4, 1.2)$ are tuned such that the system assumes the coexistence region of all chimeras, with addition of synchronous rotation state. In the beginning, after a short transient time, initial conditions result in system to assume chimera state $Z: \ (1:1:0)$. Upon receiving the first perturbation I_1 for effective $t = 10s$ of simulation time units, system changes its state and assumes the chimera state $Y: \ (1:0:0)$. The second perturbation I_2 changes the state to $X: \ (1:2:2)$.

In order to analyze the "history" dependency of the sequences and complexity level of the attractor network, three different initialization of the system are realized, Fig. 3.8. The short-lived 20s perturbation I_1 is inserted for all initializations between 200s time intervals, resulting in nine letter sequences

$$X^3 \ X^3 \ Z^2 \ Z^3 \ Y^2 \ X^1 \ Y^3 \ X^2 \ Z^3, \tag{3.2}$$
$$X^1 \ Z^3 \ Y^2 \ Y^2 \ Z^2 \ Z^2 \ Z^1 \ Z^3 \ Y^2, \tag{3.3}$$
$$Z^1 \ Y^3 \ X^1 \ Y^3 \ Z^1 \ Y^2 \ Z^3 \ Z^3 \ Y^1, \tag{3.4}$$

such that the superscript of each chimera identifies the one pendula that assumes different frequency than the other two. The first two initialization are just two different copies of chimera X while the third starts at chimera Z. Different copies of the same chimera result in different sequence for the same input. It is intuitive that copies of the same chimera state will result in different switches since the same perturbation vector pushes different pendulum in the cluster. Further analysis of the short sequences reveals that switching process is not random and certain chimera sequences emerge: for

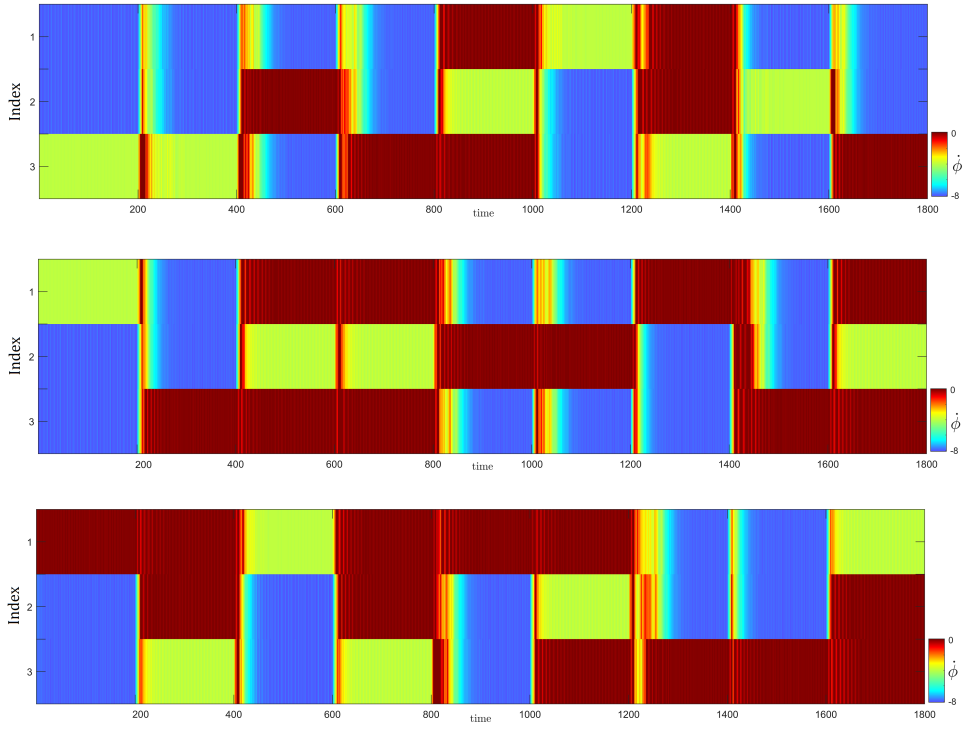

Figure 3.8: System response as switching between the chimeras to the short-lived input pulse I_1 at 200s intervals resulting in a nine letter sequence composed of chimeras. Each sequence is initialized with a different chimera state (the top two only different copies of the same cluster chimera). Upon receiving the input, each initialization results in a distinct sequence.

example Z^3 is followed by Y^2 in (3.2) and (3.3), while in (3.4) a different copy Y^1 is reached.

3.3 *Summary*

In this chapter, we introduced the coexisting chimera states as a network of attractors that are connected in the dynamical space. Some dynamical and topological properties of this network of attractors are qualitatively discussed for the minimal network $N = 3$. For information processing and neural computation, chimera network can be used in the context of LSM of reservoir computing. Although chimera states are not transient states (as proposed for LSM), the existence of chimera network allows for computation in the form of sequences of chimeras upon receiving temporally coded information instead of the system dynamics being driven by the input. This allows for a direct link to the firing patterns of neurons with temporal stimuli. Moreover, due to the tuning capability of pendula network, the same system may operate in different dynamical regimes depending on the task at hand. This property can be best illustrated comparing the pendula reservoir to a violin. Four strings of a violin maintain the same tuning for any piece the musician plays, and the music is comprised of different sequence of the notes. Different dynamical regimes may be represented by the violinist using the bow or pizzicato.

Each attractor can realize an associative memory. It is worth noting that, the chimera attractors may be used as associative memory in a "static" manner, as in the Hopfield networks. In this case, tuning the system parameters to the multistability region is not as important if the system is input driven, since the input will push the system to the attractors. The pendula-type network then will not operate different than the conventional Hopfield networks, although in limit cycle regime. The chimera network, on the other hand, is composed of chimera states in which there exists at least one limit cycle (spiking neuron).

Chapter 4

Model-in-the-loop Experiment

After the theoretical discovery of the chimera states (Kuramoto and Battogtokh [2002], Abrams and Strogatz [2004]), the experimental verification of existence of such spatio-temporal patterns in real world has been observed in coupled-map lattice (Hagerstrom et al. [2012]), hierarchical metronome networks (Martens et al. [2013]), time-delayed lasers (Larger et al. [2015]), and mechanically coupled metronomes (Kapitaniak et al. [2014]).

In this chapter, we discuss the details of the model-in-the-loop experimental setup of the electro-magnetically coupled metronomes (Ebrahimzadeh et al. [2020]) and direct numerical and experimental results are presented. In contrast to the previous experiments, the phase-lag of the kuramoto coupling function is exactly implemented, and the setup supports online control of the coupling parameters. Moreover, we confirm the smallest chimera states (Maistrenko et al. [2017]) predicted for the minimal network of Kuramoto oscillators with inertia.

4.0.1 The setup

The setup is shown schematically in Fig. 4.1, contains three standard mechanical metronomes, with their pendula rod of length l, mass m and moment of inertia B. The position of each metronome's rod is registered by an arrangement of 7 Hall sensors. For creation of a strong magnetic signal, a small Neodymium magnet is mounted on the rod. Based on the signals of the Hall sensors, the rod angle θ_i is then calculated by interpolation of a look-up table which is created in advance per calibration procedure. The coupling force is generated by an electrical current passing through the coils attached on both sides of the counter weight, the current being proportional to the respective coupling term. This method of implementation allows for

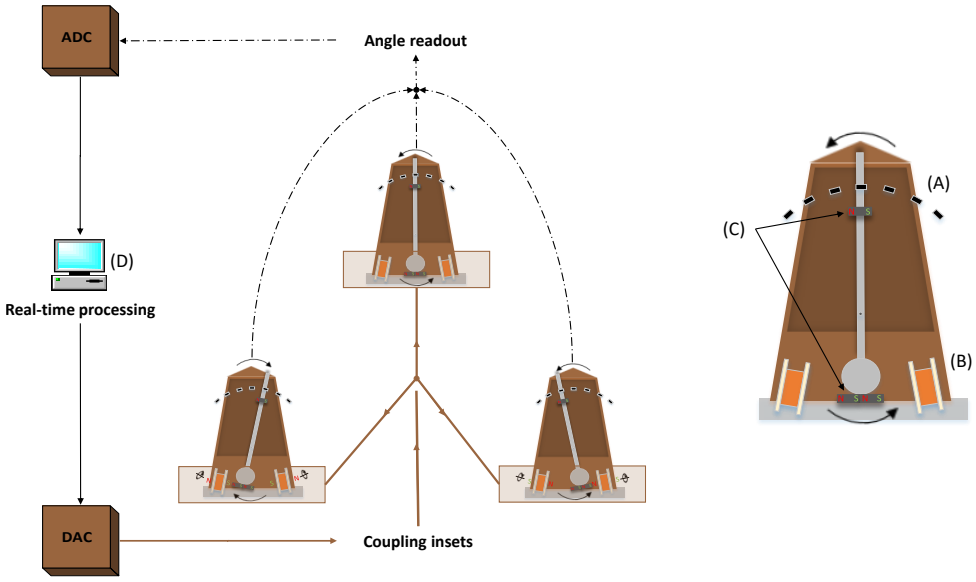

Figure 4.1: The three metronomes are equipped with an array of magnetic sensors (Hall sensors, A) for contactless measuring of the rod's position and two coils (B) for applying magnetic force onto the counter weight. To increase magnetic signal and force Neodymium magnets are attached to rod and counterweight (C). Hall sensor signals (dashed line) are digitized in the ADC unit. In real-time processing unit (D), the angles of all metronomes are reconstructed based on the ADC data and the coupling terms are calculated according to Eq. 4.1. In DAC unit the coupling terms are converted to electrical currents (solid brown lines) passing through the coils and generating magnetic forces. (See Appendix)

flexible definition and online variation of coupling strength μ and phase-lag α. Moreover, this real-time computation-implementation coupling mechanism ensures a fixed response time well below $1ms$.

The motion of each pendulum is damped by the linear damper characterized by the coefficient ε. To oppose this damping, the internal escapement mechanism of the metronome generates an excitation torque M_D in the threshold region $(-\gamma_N, \gamma_N)$: in the first stage when $0 < \theta_i < \gamma_N$ the escapement mechanism activates and $M_D = M_N$, and when $\theta_i < 0$ it is deactivated $M_D = 0$. Similarly, in the second stage for $-\gamma_N < \theta_i < 0$ activation works as $M_D = -M_N$, and for $\theta_i > 0$ $M_D = 0$.

An important characteristic of each metronome is the multistability of its dynamics. Beyond the standard oscillatory regime given by a limit cycle, there are two silent states corresponding to stable fixed points A^+, A^- $(\pm \sin^{-1} M_N/mgl, 0)$. Depending on the initial angle $\theta_{i,0}$ and the initial ve-

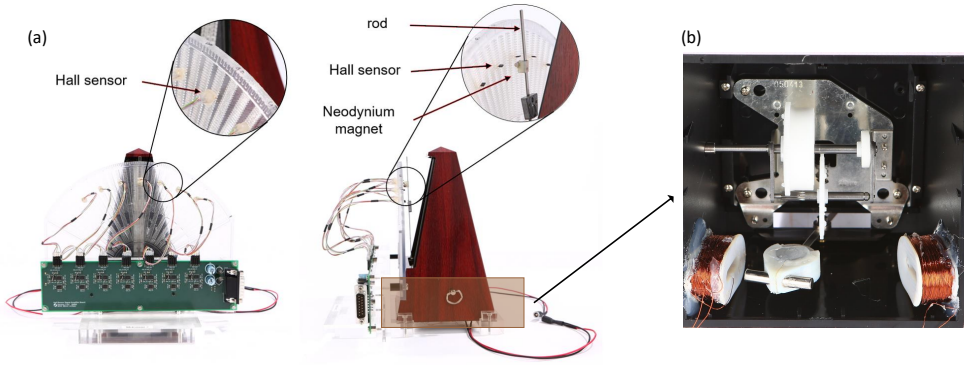

Figure 4.2: (a) angle readout of metronome using 7 Hall sensors on the sensor holder. (b) coupling implementation mechanisms (bottom view) using coils and magnet. The coupling force is effective as magnet enters coils.

locity $\dot{\theta}_{i,0}$, each of the three regimes can be realized. If $|\theta_{i,0}| > \gamma_N$ the dynamics is always oscillatory, otherwise the trajectory is over-damped as soon as phase point $(\theta_{i,0}, \dot{\theta}_{i,0})$ lie inside the ellipsoid $\theta_{i,0}/{\gamma_N}^2 + \dot{\theta}_{i,0}/\omega{\gamma_N}^2 = 1$.

The dynamics of the three-metronome system in Fig. 4.1 is modeled using the equations of motion derived from the principles of classical mechanics. The angle dynamics is then described by the pendulum equation

$$B\ddot{\theta}_i + \varepsilon\dot{\theta}_i + mgl\sin\theta_i = M_D + H(\theta_i - \theta^*)\frac{\mu}{3}\sum_{i=1}^{3}\sin(\theta_j - \theta_i - \alpha), \qquad (4.1)$$

in which the coupling term is controlled by the Heaviside step function $H(\theta - \theta^*)$ according to the position of the coils $\theta^* \approx 30^\circ$. The experiments and numerical simulation consisted of varying the coupling strength μ and phase-lag α.

4.0.2 Results

Our main result consists in the experimental observation of chimera states for the network of three all-to-all coupled metronomes. In the "chimeric" behavior, two of the metronomes are frequency synchronized in anti-phase (normally with a breathing) but the third one exhibits a different average frequency, satisfying thereby the definition of *w*eak chimera state (Ashwin and Burylko [2015]). Typical example of the experimental chimera state is presented in Fig. 4.3(left panel). The reconstructed metronome angels are presented in Fig. 4.3(a) such that the metronomes 2 & 3 are phase-locked with $\pi/2$ phase difference, while the metronome 1 is drifting. Fig. 4.3(c)

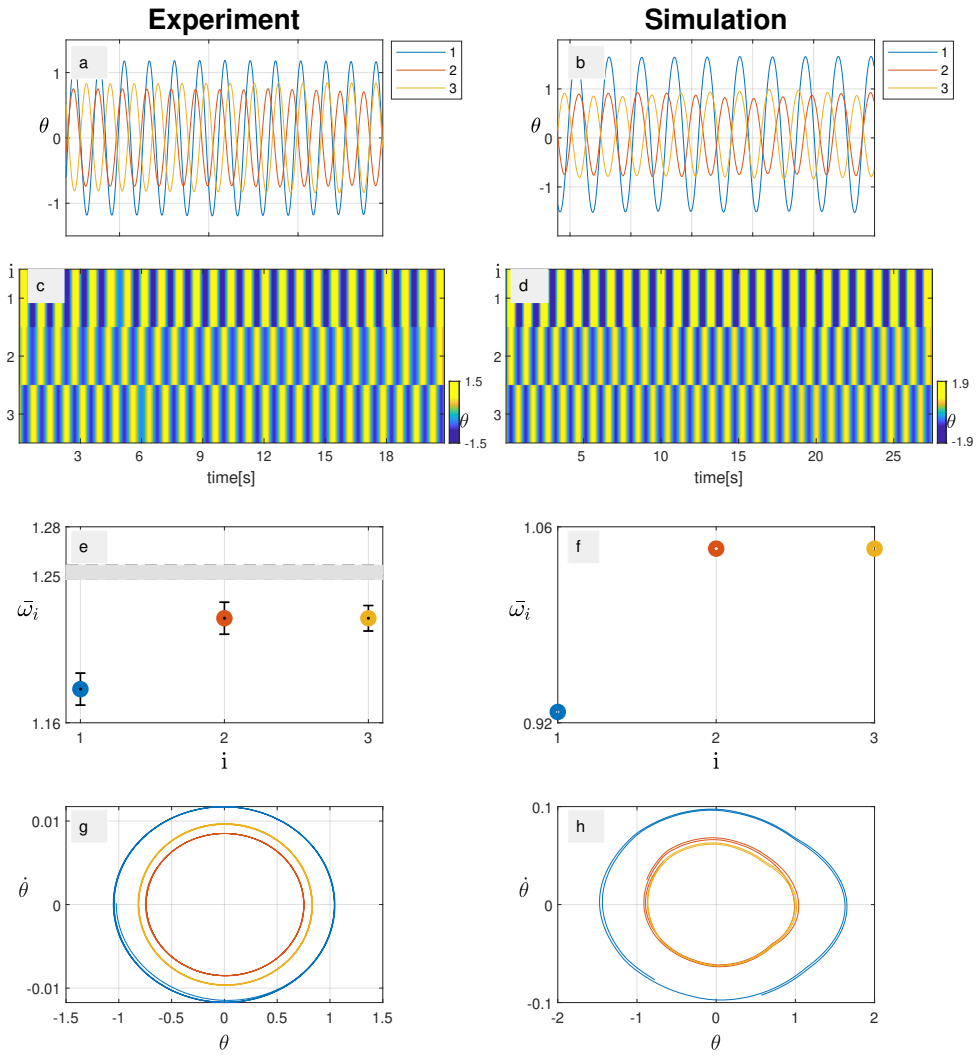

Figure 4.3: Chimera state in coupled metronome system at parameters $\alpha = 1.5$ and $\mu = 9 \times 10^{-2}$, for experiment (left) and simulation (right). (a),(b) Angle time series of metronomes showing the phase-locked metronomes no. 2 and 3, while no.1 changes its state, i.e. drifts in phase. (c),(d) color map representation of (a) and (b), respectively. (e),(f) frequency profiles showing the difference between phase-locked and drifting metronomes indicating system to be in *w*eak chimera state. The eigenfrequency of metronomes reside in the gray region of (g) where their difference is calibrated less than 1%. (g),(h) phase portraits of approximately two periods of time interval of (a) and (b).

shows the colormap of the rod angel for longer time span. Furthermore, the average frequency of the metronomes are presented Fig. 4.3(e): metronomes 2 & 3 have the same frequency while metronome 1 is oscillating slower. The gray bar notes the average frequency of the uncoupled metronome. Finally, phase portraits of the metronome trajectories showing a periodic motion Fig. 4.3(g). The corresponding simulation results are presented in Fig. 4.3(right panel). The state is obtained for practically identical metronomes (natural frequencies are calibrated for less than 1% deviations), and fully symmetric coupling strength controlled by the computer. We find that this kind chimeras arise at large enough values of the phase-lag parameter α, beginning from $\alpha \approx 0.7$, and they preserve with further increase of α, even beyond $\pi/2$. Robustness of the experimental chimeras is additionally supported by the fact that they originate from arbitrary assigned initial conditions (as long as all three metronomes are in the oscillatory regime).

Full parameter region for the dynamical behavior of system (4.1) is presented in Fig. 4.4. For small values of phase-lag α, the metronomes are in full synchronization. Increasing α, the system undergoes a symmetry break manifested as switchings between synchronous state. The switching are short-lived weak chimeras that are transversally unstable. Further increase of α in the gray region, the chimera states are stable and globally attractive. Beyond the gray region for bigger α, chimeras lose stability and the dominant dynamics are rotating waves, in which no stable group of synchronous metronomes exists.

An example of the switching state in both experiment and simulation is exhibited in Fig. 4.4 for $\alpha = 0.95$. The synchronous state is the long-period dominant dynamics of the system, coexisting with saddle chimeras. At an arbitrary time, system trajectory may leave the synchronous state and fall into a chimera state via their stable manifold. The chimera is transversally unstable, hence after a short period, the trajectory is repelled out of the chimera's unstable manifold. It may be that, several of such heteroclinic switches happen before the trajectory settling in the synchronous state. Near the boundary of the blue *switching* region and the synchronous state, the switches are rare events. With increase of α, the probability of switches increases until the chimeras become stable. Beyond $\pi/2$, chimeras lose transverse stability and the heteroclinic switches coexist with the rotating waves.

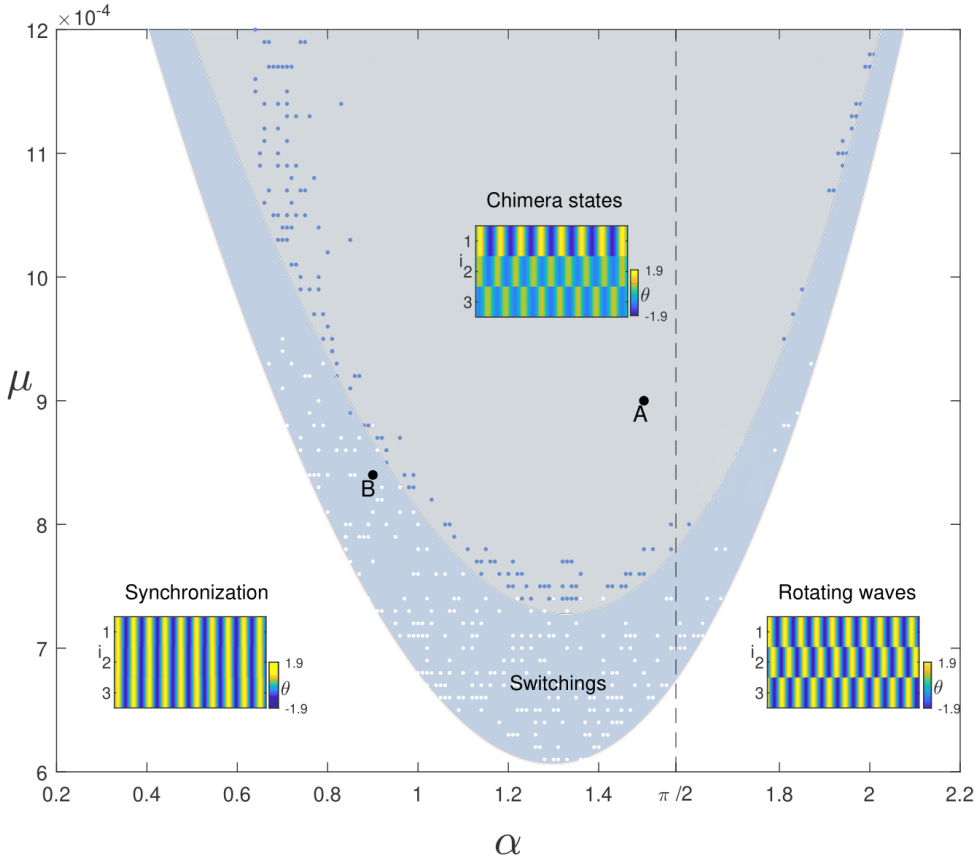

Figure 4.4: Parameter region of dependence of different spatio-temporal patterns on parameters α and μ. The white data points in the *S*witchings region indicate coexistence of the synchronous state (for $\alpha < \pi/2$) and rotating waves (for $\alpha > \pi/2$) with heteroclinic switchings. The border between Chimera states and *S*witchings are not clear cut, heteroclinic switchings infiltrated the chimera region are shown as blue dots. The sample points A and B are presented in Figs. 4.3 and 4.5, respectively.

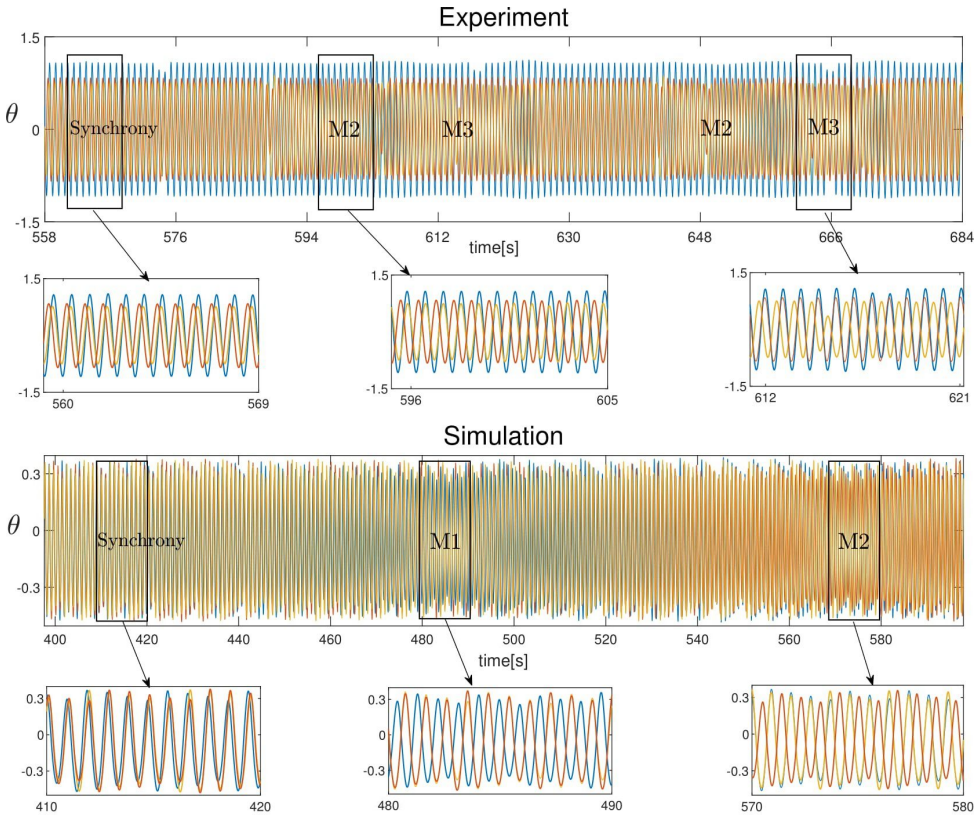

Figure 4.5: Heteroclinic switchings corresponding to data point *B* in parameter region Fig. 4.4 in experiment (up) and simulation (down). The intervals in which metronomes makes a phase slip are labeled with number of the metronome.

Chapter 5

Conclusion

This thesis provides a systematic investigation into synchronization phenomena in coupled nonlinear dynamical systems, focusing on the emergence of complex collective behaviors in networks of excitable elements. Using fundamental models of coupled pendula networks, we demonstrate and analyze emergence of chimera states as nontrivial, counterintuitive network attractors, their multiplicity, and noise/input-driven switching dynamics between the chimeras. Our findings contribute to the current research in nonlinear dynamics, both by uncovering new emergent behaviors and by providing a detailed analysis of their structural and stability properties across various network sizes. In addition, the study of minimal metronome network in controlled experimental settings confirms the existence of chimera states in real world systems. Taken together, these results lay a foundation for advancing our capacity to understand, model, and potentially leverage these mechanisms in the context of neural computation. Thus, this thesis contributes new insights to the field of complex systems and nonlinear dynamics, with implications for future applications in neuromorphic computing, bio-inspired network design, and the broader study of biological and engineered systems. Let us summarize the scientific contributions of this thesis.

Chimera states as frequency clustering in the oscillator networks.

The chimera states refer to coexistence of synchronous and incoherent states in network of identical oscillators [Kuramoto and Battogtokh, 2002, Abrams and Strogatz, 2004]. In this thesis, we identified chimera states that are in the form of distinct clusters separated by their average frequency, where the dynamics of each cluster lies on a synchronous manifold. This is in contrast to the incoherent group of the traditional chimera states. The frequency clustering is related to the addition of the inertia to the oscillators, and the oscillator model recovers the pendulum equation.

Multiplicity of the chimera states.

The traditional chimera states in standard Kuramoto model are chaotic transient sets [Wolfrum and Omel'chenko, 2011]. In the pendulum network, however, different clustering formation are found to coexist for the same set of coupling parameters. In this multiplicity regions, the final behavior of the system is determined by the initial conditions.

Conceptual methods for hardware-implemented computation.

In the context of bio-inspired computation away from the von Neumann architecture, networks of coupled oscillators are one of the candidates [Rovelli, 2022, Delacour et al., 2023, Woo et al., 2024]. We studied the collective dynamics and coupling effects in paradigmatic pendula networks. To that end, the network attractors, chimera states, are similar to the attractor states in Hopfield networks [Hopfield, 1982], but in the limit cycle regime. Our study serves as a foundation for designing coupled oscillator networks optimized for computation, using network attractors as functional elements for processing information.

Experimental verification of chimera states.

We have provided the experimental setup of coupled metronomes, whose dynamics are identical to that of pendulum. The setup configuration allows for exact implementation of the coupling parameters phase-shift and coupling strength that are used in theoretical study. Chimera states are observed for the same set of coupling parameters predicted by the numerical simulations of metronome equation.

5.1 *Outlook*

The results of the pendulum network may be extended beyond the phase-shift $\alpha > \pi/2$, where the chimeras are reported to become chaotic [Brezetsky et al., 2021b].

The pendula network are dissipative systems away from thermodynamic equilibrium, the emergence of chaotic states are expected. The clustering of the chimeras, however, indicates an underlying physical law that enables for the formation of the synchronous manifolds. As shown in the section (2.4), the phase-shift becomes the pendula torque as a result of synchronization. This torque then allows for pendula rotation. The physical implication of the phase-shift parameter need to be fully understood. The hypothesis is that, phase-shift acts as energy source such that the coupling

function is a locally active element. Recently, active signal transmission in $LaCoO_3$ material [Brown et al., 2024] has been reported allowing for lossless interaction in dissipative systems. The underlying physical law of this phenomenon is the entropy production minimizations.

In the thesis, we limited the theory to the globally connected networks. The study needs to be extended for various network structures where the interplay between the element dynamics, structure and coupling function are non-negligible [Schülen et al., 2022]. In reference Gerster et al. [2020], for example, episodes of brain seizures are modeled in oscillator networks with small-world structure.

Finally, the author hopes to develop a nonextensive statistical mechanics formalism [Tsallis, 1988, Abe and Okamoto, 2001] for the dissipative systems of coupled oscillators.

Bibliography

Sumiyoshi Abe and Yuko Okamoto. *Nonextensive statistical mechanics and its applications*, volume 560. Springer Science & Business Media, 2001.

Daniel M. Abrams and Steven H. Strogatz. Chimera states for coupled oscillators. *Phys. Rev. Lett.*, 93:174102, Oct 2004. doi: 10.1103/PhysRevLett.93.174102.

II Arikpo, FU Ogban, and IE Eteng. Von neumann architecture and modern computers. *Global Journal of Mathematical Sciences*, 6(2):97–103, 2007.

Peter Ashwin and Oleksandr Burylko. Weak chimeras in minimal networks of coupled phase oscillators. *Chaos: An Interdisciplinary Journal of Nonlinear Science*, 25(1), 2015.

Joseph Auslander, Nam P Bhatia, and Peter Seibert. Attractors in dynamical systems. Technical report, 1964.

Iva Bačić. *Self-organization in coupled excitable systems: interplay between multiple timescale dynamics and noise*. 2020.

Igor V Belykh, Barrett N Brister, and Vladimir N Belykh. Bistability of patterns of synchrony in kuramoto oscillators with inertia. *Chaos: An Interdisciplinary Journal of Nonlinear Science*, 26(9), 2016.

Serhiy Brezetsky, Patrycja Jaros, Roman Levchenko, Tomasz Kapitaniak, and Yuri Maistrenko. Chimera complexity. *Phys. Rev. E*, 103:L050204, May 2021a. doi: 10.1103/PhysRevE.103.L050204.

Serhiy Brezetsky, Patrycja Jaros, Roman Levchenko, Tomasz Kapitaniak, and Yuri Maistrenko. Chimera complexity. *Physical Review E*, 103(5): L050204, 2021b.

Per Brodal. *The central nervous system: structure and function*. oxford university Press, 2004.

Eric Brown, Jeff Moehlis, and Philip Holmes. On the phase reduction and response dynamics of neural oscillator populations. *Neural computation*, 16(4):673–715, 2004.

Timothy D Brown, Alan Zhang, Frederick U Nitta, Elliot D Grant, Jenny L Chong, Jacklyn Zhu, Sritharini Radhakrishnan, Mahnaz Islam, Elliot J Fuller, A Alec Talin, et al. Axon-like active signal transmission. *Nature*, pages 1–7, 2024.

Andrea Ceni, Peter Ashwin, and Lorenzo Livi. Interpreting recurrent neural networks behaviour via excitable network attractors. *Cognitive Computation*, 12(2):330–356, 2020.

Albert Compte. Computational and in vitro studies of persistent activity: edging towards cellular and synaptic mechanisms of working memory. *Neuroscience*, 139(1):135–151, 2006.

Peter Dayan and Laurence F Abbott. *Theoretical neuroscience: computational and mathematical modeling of neural systems*. MIT press, 2005.

Corentin Delacour, Stefania Carapezzi, Gabriele Boschetto, Madeleine Abernot, Thierry Gil, Nadine Azemard, and Aida Todri-Sanial. A mixed-signal oscillatory neural network for scalable analog computations in phase domain. *Neuromorphic Computing and Engineering*, 3(3):034004, 2023.

P Ebrahimzadeh, M Schiek, and Y Maistrenko. Mixed-mode chimera states in pendula networks. *Chaos: An Interdisciplinary Journal of Nonlinear Science*, 32(10), 2022.

Pezhman Ebrahimzadeh, Michael Schiek, Patrycja Jaros, Tomasz Kapitaniak, Stefan van Waasen, and Yuri Maistrenko. Minimal chimera states in phase-lag coupled mechanical oscillators. *The European Physical Journal Special Topics*, 229:2205–2214, 2020.

John Carew Eccles. *The physiology of synapses*. Academic Press, 2013.

G. B. Ermentrout and N. Kopell. Parabolic bursting in an excitable system coupled with a slow oscillation. *SIAM Journal on Applied Mathematics*, 46 (2):233–253, 1986. doi: 10.1137/0146017.

Moritz Gerster, Rico Berner, Jakub Sawicki, Anna Zakharova, Antonín Škoch, Jaroslav Hlinka, Klaus Lehnertz, and Eckehard Schöll. Fitzhugh–nagumo oscillators on complex networks mimic epileptic-seizure-related synchronization phenomena. *Chaos: An Interdisciplinary Journal of Nonlinear Science*, 30(12), 2020.

Richard Janis Goldschmidt, Arkady Pikovsky, and Antonio Politi. Blinking chimeras in globally coupled rotators. *Chaos: An Interdisciplinary Journal of Nonlinear Science*, 29(7), 2019.

Boris S Gutkin, G Bard Ermentrout, and Alex D Reyes. Phase-response curves give the responses of neurons to transient inputs. *Journal of neurophysiology*, 94(2):1623–1635, 2005.

Aaron M Hagerstrom, Thomas E Murphy, Rajarshi Roy, Philipp Hövel, Iryna Omelchenko, and Eckehard Schöll. Experimental observation of chimeras in coupled-map lattices. *Nature Physics*, 8(9):658–661, 2012.

Georg Wilhelm Friedrich Hegel and Michael Inwood. *Hegel: philosophy of mind: translated with introduction and commentary*. Oxford University Press, 2007.

Moritz Helias and David Dahmen. *Statistical field theory for neural networks*, volume 970. Springer, 2020.

Morris W Hirsch and Bill Baird. Computing with dynamic attractors in neural networks. *Biosystems*, 34(1-3):173–195, 1995.

John J Hopfield. Neural networks and physical systems with emergent collective computational abilities. *Proceedings of the national academy of sciences*, 79(8):2554–2558, 1982.

Frank C Hoppensteadt and Eugene M Izhikevich. *Weakly connected neural networks*, volume 126. Springer Science & Business Media, 1997.

Tomasz Kapitaniak, Patrycja Kuzma, Jerzy Wojewoda, Krzysztof Czolczynski, and Yuri Maistrenko. Imperfect chimera states for coupled pendula. *Scientific reports*, 4(1):6379, 2014.

Mikail Khona and Ila R Fiete. Attractor and integrator networks in the brain. *Nature Reviews Neuroscience*, 23(12):744–766, 2022.

Arndt Klotz and Kurt Bräuer. A small-size neural network for computing with strange attractors. *Neural Networks*, 12(4-5):601–607, 1999.

Yoshiki Kuramoto and Dorjsuren Battogtokh. Coexistence of coherence and incoherence in nonlocally coupled phase oscillators. *Nonlinear Phenom. Complex Syst. 5, 380–385*, 2002.

Yuri A Kuznetsov, Iu A Kuznetsov, and Y Kuznetsov. *Elements of applied bifurcation theory*, volume 112. Springer, 1998.

Carlo R Laing and Carson C Chow. Stationary bumps in networks of spiking neurons. *Neural computation*, 13(7):1473–1494, 2001.

Carlo R Laing, William C Troy, Boris Gutkin, and G Bard Ermentrout. Multiple bumps in a neuronal model of working memory. *SIAM Journal on Applied Mathematics*, 63(1):62–97, 2002.

Laurent Larger, Bogdan Penkovsky, and Yuri Maistrenko. Laser chimeras as a paradigm for multistable patterns in complex systems. *Nature communications*, 6(1):7752, 2015.

S. Lek and Y.S. Park. Artificial neural networks. In Sven Erik Jørgensen and Brian D. Fath, editors, *Encyclopedia of Ecology*, pages 237–245. Academic Press, Oxford, 2008.

Otto Loewi. Chemical transmission of nerve impulses. *American Scientist*, 33(3):159–174, 1945.

Mantas Lukoševičius and Herbert Jaeger. Reservoir computing approaches to recurrent neural network training. *Computer Science Review*, 3(3):127–149, 2009. ISSN 1574-0137. doi: https://doi.org/10.1016/j.cosrev.2009.03.005.

Francisco López-Muñoz, Jesús Boya, and Cecilio Alamo. Neuron theory, the cornerstone of neuroscience, on the centenary of the nobel prize award to santiago ramón y cajal. *Brain Research Bulletin*, 70(4):391–405, 2006. ISSN 0361-9230. doi: https://doi.org/10.1016/j.brainresbull.2006.07.010.

Wolfgang Maass, Thomas Natschläger, and Henry Markram. Real-time computing without stable states: A new framework for neural computation based on perturbations. *Neural computation*, 14(11):2531–2560, 2002.

Misha Mahowald and Carver Mead. The silicon retina. *An Analog VLSI System for Stereoscopic Vision*, pages 4–65, 1994.

Yuri Maistrenko, Serhiy Brezetsky, Patrycja Jaros, Roman Levchenko, and Tomasz Kapitaniak. Smallest chimera states. *Physical Review E*, 95(1): 010203, 2017.

Erik Andreas Martens, Shashi Thutupalli, Antoine Fourriere, and Oskar Hallatschek. Chimera states in mechanical oscillator networks. *Proceedings of the National Academy of Sciences*, 110(26):10563–10567, 2013.

C. Mead. Neuromorphic electronic systems. *Proceedings of the IEEE*, 78(10): 1629–1636, 1990. doi: 10.1109/5.58356.

Akira Miyake, Priti Shah, et al. *Models of working memory*. Citeseer, 1999.

Bharat Monga, Dan Wilson, Tim Matchen, and Jeff Moehlis. Phase reduction and phase-based optimal control for biological systems: a tutorial. *Biological cybernetics*, 113(1-2):11–46, 2019.

Kohei Nakajima and Ingo Fischer. *Reservoir Computing*. Springer, 2021.

Aljoscha C. Neubauer and Andreas Fink. Intelligence and neural efficiency. *Neuroscience and Biobehavioral Reviews*, 33(7):1004–1023, 2009.

NF Pedersen, OH Soerensen, B Dueholm, and J Mygind. Half-harmonic parametric oscillations in josephson junctions. *Journal of Low Temperature Physics*, 38(1):1–23, 1980.

Bastian Pietras and Andreas Daffertshofer. Network dynamics of coupled oscillators and phase reduction techniques. *Physics Reports*, 819:1–105, 2019. ISSN 0370-1573. doi: https://doi.org/10.1016/j.physrep.2019.06.001. Network dynamics of coupled oscillators and phase reduction techniques.

Mikhail I Rabinovich, Michael A Zaks, and Pablo Varona. Sequential dynamics of complex networks in mind: Consciousness and creativity. *Physics Reports*, 883:1–32, 2020.

John Rinzel and G Bard Ermentrout. Analysis of neural excitability and oscillations. *Methods in neuronal modeling*, 2:251–292, 1998.

Carlo Rovelli. Memory and entropy. *Entropy*, 24(8):1022, 2022.

Hidetsugu Sakaguchi and Yoshiki Kuramoto. A soluble active rotater model showing phase transitions via mutual entertainment. *Progress of Theoretical Physics*, 76(3):576–581, 1986.

Jannis Schuecker, Sven Goedeke, and Moritz Helias. Optimal sequence memory in driven random networks. *Phys. Rev. X*, 8:041029, Nov 2018. doi: 10.1103/PhysRevX.8.041029.

Leonhard Schülen, Maria Mikhailenko, Everton S Medeiros, and Anna Zakharova. Solitary states in complex networks: impact of topology. *The European Physical Journal Special Topics*, 231(22):4123–4130, 2022.

JC Sprott. Chaotic dynamics on large networks. *Chaos: An Interdisciplinary Journal of Nonlinear Science*, 18(2), 2008.

Steven H Strogatz. *Nonlinear dynamics and chaos with student solutions manual: With applications to physics, biology, chemistry, and engineering*. CRC press, 2018.

Botond Szatmáry and Eugene M Izhikevich. Spike-timing theory of working memory. *PLoS computational biology*, 6(8):e1000879, 2010.

Constantino Tsallis. Possible generalization of boltzmann-gibbs statistics. *Journal of statistical physics*, 52:479–487, 1988.

Alan M. Turing. *Computing Machinery and Intelligence*, pages 23–65. Springer Netherlands, Dordrecht, 2009.

Sacha J. van Albada, Andrew G. Rowley, Johanna Senk, Michael Hopkins, Maximilian Schmidt, Alan B. Stokes, David R. Lester, Markus Diesmann, and Steve B. Furber. Performance comparison of the digital neuromorphic hardware spinnaker and the neural network simulation software nest for a full-scale cortical microcircuit model. *Frontiers in Neuroscience*, 12, 2018.

John Von Neumann and Ray Kurzweil. *The computer and the brain*. Yale university press, 2012.

Robert W Williams and Karl Herrup. The control of neuron number. *Annual review of neuroscience*, 11(1):423–453, 1988.

Klaus Wimmer, Duane Q Nykamp, Christos Constantinidis, and Albert Compte. Bump attractor dynamics in prefrontal cortex explains behavioral precision in spatial working memory. *Nature neuroscience*, 17(3):431–439, 2014.

Arthur T Winfree. Biological rhythms and the behavior of populations of coupled oscillators. *Journal of theoretical biology*, 16(1):15–42, 1967.

Matthias Wolfrum and Oleh E Omel'chenko. Chimera states are chaotic transients. *Physical Review E—Statistical, Nonlinear, and Soft Matter Physics*, 84(1):015201, 2011.

Kyung Seok Woo, Hyungjun Park, Nestor Ghenzi, A Alec Talin, Taeyoung Jeong, Jung-Hae Choi, Sangheon Oh, Yoon Ho Jang, Janguk Han, R Stanley Williams, et al. Memristors with tunable volatility for reconfigurable neuromorphic computing. *ACS Nano*, 2024.

S Ramón y Cajal. Histologie du systeme nerveux de l'homme et des vertebre´ s ii. *(No Title)*, 1909.

Yuanzhao Zhang, Zachary G. Nicolaou, Joseph D. Hart, Rajarshi Roy, and Adilson E. Motter. Critical switching in globally attractive chimeras. *Phys. Rev. X*, 10:011044, Feb 2020. doi: 10.1103/PhysRevX.10.011044.

Jean Zinn-Justin. *Quantum field theory and critical phenomena*, volume 171. Oxford university press, 2021.